

# The woolly rhinoceros (*Coelodonta antiquitatis*) from Ondorkhaan, eastern Mongolia

NAOTO HANDA , MASAMI IZUHO , KEIICHI TAKAHASHI, FUMIE IIZUKA , BATMUNKH TSOGTBAATAR, BYAMBAA GUNCHINSUREN , DAVAKHUU ODOSUREN AND LOCHIN ISHITSEREN 

**BOREAS**



Handa, N., Izuho, M., Takahashi, K., Iizuka, F., Tsogtbaatar, B., Gunchinsuren, B., Odosuren, D. & Ishitseren, L.: The woolly rhinoceros (*Coelodonta antiquitatis*) from Ondorkhaan, eastern Mongolia. *Boreas*. <https://doi.org/10.1111/bor.12582>. ISSN 0300-9483.

The Mammoth Faunas, the famous cold-adapted mammal assemblages, were distributed widely across northern Eurasia and North America during the Late Pleistocene. The now extinct woolly rhinoceros, *Coelodonta antiquitatis*, was a major component. Abundant fossil remains of this species with radiocarbon dates have been reported through almost all of northern Eurasia, but the fossil rhinoceroses of Mongolia are poorly known. Here, we describe a rhinocerotid skeleton from Ondorkhaan, eastern Mongolia, and compare it with four Late Pleistocene rhinoceros species of northern Eurasia (*Elasmotherium sibiricum*, *Stephanorhinus hemitoechus*, *Stephanorhinus kirchbergensis* and *C. antiquitatis*), resulting in its identification as a woolly rhinoceros (*C. antiquitatis*). Accelerator mass spectrometry radiocarbon dates obtained from two samples (ODK01 and ODK02) of the skeleton essentially agree, 42 160–40 040 cal. a BP and 42 105–39 955 cal. a BP, and the two samples had  $\delta^{13}\text{C}$  values of  $-19.5\text{‰}$  and  $-20.2\text{‰}$  SMMKW, respectively. This find suggests that the Mammoth Faunas were distributed in eastern Mongolia c. 45–40 ka during the period of climatic amelioration between Heinrich events 5 (H5: 46 000 cal. a BP) and 4 (H4: 39 000 cal. a BP).

*Naoto Handa* ([k1552325@kadai.jp](mailto:k1552325@kadai.jp)) and *Masami Izuho*, Faculty of Social Sciences and Humanities, Tokyo Metropolitan University, Minami-Osawa 1-1, Hachioji, Tokyo 192-0397, Japan; *Keiichi Takahashi*, Lake Biwa Museum, 1091, Oroshimo, Kusatsu, Shiga 525-0001, Japan; *Fumie Iizuka*, Department of Anthropology and Heritage Studies, University of California, Merced, Classroom and Office Building, 5200 North Lake Road, Merced, CA95343, USA; *Batumunkh Tsogtbaatar*, *Byambaa Gunchinsuren*, *Davakhuu Odosuren* and *Lochin Ishitseren*, Institute of Archaeology, Mongolian Academy of Sciences, Jucov Street-77, Ulaanbaatar-51, Mongolia; received 7th June 2021, accepted 24th December 2021.

The woolly rhinoceros, *Coelodonta antiquitatis*, a major member of the Mammoth Faunas, was most widespread in northern Eurasia during the Marine Isotope Stage 3 (MIS 3; e.g. Markova & Puzachenko, 2007; Stuart & Lister 2012). The southern margin of its distributional range spans from Spain to southern Siberia and onward to Inner Mongolia and northeastern and eastern China (Takahashi *et al.* 2007; Álvarez-Lao & García 2011; Dong *et al.* 2014; Kahlke 2014; Álvarez-Lao *et al.* 2017). Stuart & Lister (2012) reviewed the radiocarbon-dated fossil records of *C. antiquitatis*, as such records are abundant in western and central Europe, Russia, Inner Mongolia, Salawusu, Ordos, Nei Menggu, and discussed the chronology of changes in its distribution. Such a study requires a large number of well-dated fossils, but despite an abundance of remains from various parts of Mongolia, the fossil rhinoceroses of Mongolia are poorly known. As a result, Stuart & Lister (2012) could not say much about the woolly rhinoceroses that may once have lived there.

To rectify this situation, taxonomic descriptions and radiocarbon dating of the Mongolian rhinoceros remains that have precise locality data are needed. Late Pleistocene rhinoceros species, such as *Elasmotherium sibiricum* and *Stephanorhinus kirchbergensis*, have been described from the Late Pleistocene deposits in northern Eurasia except for woolly rhino (e.g. Kirillova *et al.* 2017; Kosintsev *et al.* 2019). Sufficiently detailed palaeontological

investigations are required in order to accept a given fossil find as a woolly rhinoceros.

During MIS 3 and the Last Glacial Maximum (LGM), the Mammoth Faunas expanded widely in northern Eurasia, both southwards and also from east to west. The southern margin of this extended range reached from Spain to southern Siberia and onwards throughout northeast China (e.g. Markova & Puzachenko, 2007; Markova *et al.* 2010; Álvarez-Lao & García 2011; Dong *et al.* 2014), and was associated with temperate conditions. Mongolia was no doubt included in this range, but the composition of the Mammoth Faunas in Mongolia is unclear. The provision of detailed descriptions and absolute dates for Late Pleistocene mammal remains from Mongolia is, therefore, an important uncompleted task.

In 2012, a rhinocerotid skeleton was discovered at Ondorkhaan in eastern Mongolia (Fig. 1), the first such find associated with precise geographical coordinates for the recovery site. No detailed descriptions of these remains have been published in the English language in a peer-reviewed journal, although a preliminarily report did appear in Japan (Handa *et al.* 2017). Here, we describe this skeleton and identify it as a woolly rhinoceros (*Coelodonta antiquitatis*). Based on accelerator mass spectrometry radiocarbon dates (hereafter, AMS  $^{14}\text{C}$  dates) obtained from this skeleton, we also discuss its archaeological and palaeobiogeographical implications.

## Material and methods

### Excavation and description

The rhinocerotid skeleton was found in silty sand and gravel beds in a Late Pleistocene alluvial fan at a construction site in Ondorkhaan City, Khenty Province, eastern Mongolia (latitude 47°19'33.57''N, longitude 110°40'1.58''E; Fig. 1). Because of the need to excavate the bones quickly, the detailed geological context of the fossil-bearing horizon was not recorded. However, many photographs were taken in the field at the fossil recovery site by curators of the Khenty Local Museum in Ondorkhaan, where the bones are now stored under the registration number H.E.M 2012.24.1.

In total, 54 skeletal remains including abundant rib bone fragments were found and described. Measurements follow Guérin (1980) and van der Made (2010), the taxonomic classification follows Antoine (2002) and Pandolfi (2018), and the anatomical terminology follows van der Made (2010) and Mallet *et al.* (2019). H.E.M 2012.24.1 was compared morphologically with three Upper Pleistocene species of the subtribe Rhinocerotina from northern Eurasia (*Stephanorhinus hemitoechus*, *Stephanorhinus kirchbergensis* and *Coelodonta antiquitatis*) and a species of the subtribe Elasmotheriina from the same time period and region (*Elasmotherium sibiricum*). To compare sizes, we compared measurements of certain limb bones (radius, McIII, MtIII and astragalus) of these four species with H.E.M 2012.24.1. We could not use the measurements of the humerus, femur and tibia because relevant data were not available for some species.

### Radiocarbon dating and $\delta^{13}\text{C}$ analysis

Two AMS  $^{14}\text{C}$  dates were obtained from bone samples from ribs of H.E.M 2012.24.1 (samples ODK01 and ODK02; Table 1). After recording the basic data for



Fig. 1. Map showing the location of the collection site at Ondorkhaan in eastern Mongolia (modified from Handa *et al.* 2017).

these samples, they were sent in June 2013 to Stafford Research Laboratories, Inc. (Lafayette, Colorado, USA) for analysis, and the dating results were obtained in July 2014. Pretreatment there was mainly based on ultrafiltration following the protocol of Waters & Stafford (2007). Samples of crushed bone were decalcified and washed, treated with 0.05 N NaOH overnight to remove humics, soaked in 0.1 N HCl, gelatinized at 60 °C at pH 2, and ultrafiltered at 30 kDa.  $\delta^{13}\text{C}$  and  $\delta^{15}\text{N}$  were measured to a precision of <0.1 and <0.2‰, respectively, on aliquots of ultrafiltered collagen, using a Fisons NA1500NC elemental analyser and a Finnigan Delta Plus isotope ratio mass spectrometer. OxCAL v4.4.2 (Bronk Ramsey 2009; Reimer *et al.* 2020) was used to calibrate the radiocarbon dates. The  $\delta^{13}\text{C}$  values were compared with other Late Pleistocene data from extinct mammals and palaeosols in southern Transbaikal, Siberia (Schwartz-Narbonne *et al.* 2019; Golubtsov 2020) in an effort to deduce the animal's habitat and diet while it was alive.

### Systematic palaeontology

Order PERISSODACTYLA Owen, 1848  
 Family RHINOCEROTIDAE Gray, 1821  
 Subfamily RHINOCEROTINAE Gray, 1821  
 Tribe RHINOCEROTINI Gray, 1821  
 Subtribe RHINOCEROTINA Gray, 1821  
 Genus *Coelodonta* Bronn, 1837

Diagnosis (after Qiu *et al.* 2004: pp. 119, 186). Large-sized rhinoceros with tandem horns. Skull is dolichocephalic, nasals are long and wide, the anterior end downturned, the bony septum is complete or almost complete and occiput is strongly or moderately backwards-slanting. Symphysis is slightly widened on the anterior rim. Upper and lower incisors are generally absent, but sometimes present in highly atrophied state in older forms; crown of cheek teeth is hypsodont, enamel surface is vermiculated and covered with cement; the ectoloph of the upper cheek teeth is wavy, with prominent para- and metacone ribs and para- and metastyles; protocone is backwards-slanting, its crochet and crista are well developed and rarely ramified; the medi- and postfossette are formed at the early stage of wear, with third molar becoming quadrangular in later forms; labial walls of lower cheek teeth are flattened, with meta- and entoconid and swollen anterior, medial and posterior ribs. Limb bones are relatively short.

*Coelodonta antiquitatis* (Blumenbach, 1799)  
 Figs 2–11, S2.

Diagnosis (after Guérin 2010: p. 701). Overall size is medium to very large. Massive facial part is very long, with ossified nasal septum uniting nasals and intermax-

Table 1.  $^{14}\text{C}$  dates for H.E.M 2012.24.1 from Ondorkhaan in eastern Mongolia.

Sample no.	Material for dating	Geological unit	Yield (‰)	$\delta^{13}\text{C}$ (‰)	Fraction dated	Lab. no.	Age ( $^{14}\text{C}$ a BP)	Calibrated age (cal. a BP, $2\sigma$ )	Context
SR-8306	Rib bone of <i>Coelodonta antiquitatis</i>	Silty sand 5 m below the ground surface.	5.4	-19.5	Ultrafiltration gelatine	UCIAMS-143223	36 190±690	42 160–40 038	ODK01, found with complete skeleton of an individual.
SR-8307	Rib bone of <i>Coelodonta antiquitatis</i>	Silty sand 5 m below the ground surface.	6.3	-20.2	Ultrafiltration gelatine	UCIAMS-143224	36 080±680	42 107–39 953	ODK02, found with complete skeleton of an individual.

illaries. Two horns, with ossified nasal horn preceding frontal horn; insertion of frontal horn is well marked as small convexity. Occipital surface extends backwards and towards dorsally; its upper part largely overhanging occipital condyles. Auditory pseudo-meatus is closed down. Front of mandible with long, enlarged symphysis, thick and high horizontal branch of mandible with

strongly convex ventral edge. Chagrined enamel cheek teeth are heavily cemented. Ectolophs of first and second molars are strongly wavy, fold of the paracone is small but clear, the crochet is always present, crista is normally present, usually with closed medifossette. Premolars are similar, but their protocone is distinguishable (especially in second premolar). Lingual cingulum is extremely rare.

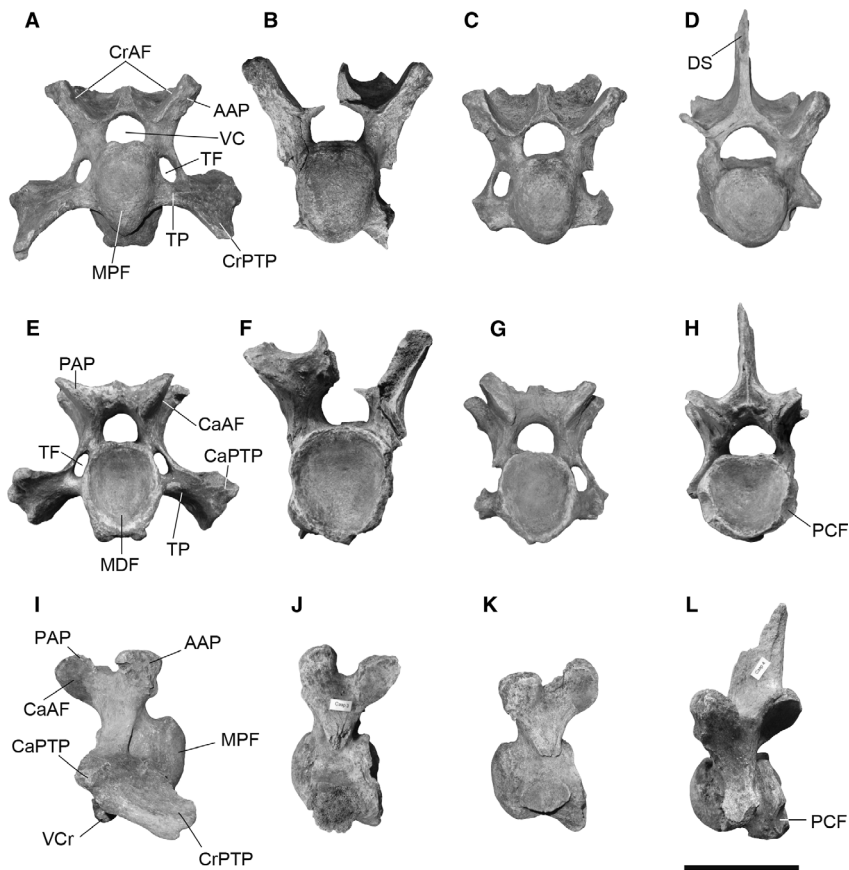


Fig. 2. Cervical vertebrae. A. Cranial view of 3rd cervical. B. Cranial view of 4th cervical. C. Cranial view of 5th cervical. D. Cranial view of 7th cervical. E. Caudal view of 3rd cervical. F. Caudal view of 4th cervical. G. Caudal view of 5th cervical. H. Caudal view of 7th cervical. I. Right side view of 3rd cervical. J. Left side view of 4th cervical. K. Left side view of 5th cervical. L. Left side view of 7th cervical. AAP = anterior articular process; CaAF = caudal articular facet; CaPTP = caudal part of the transverse process; CrAF = cranial articular facet; CrPTP = cranial part of the transverse process; DS = dorsal spine; MDF = main distal facet; MPF = main proximal facet; PAP = posterior articular process; PCF = posterior costal facet, TF = transverse foramen; TP = transverse process; VC = vertebral canal; VCr = ventral crest. Scale bar represents 10 cm.

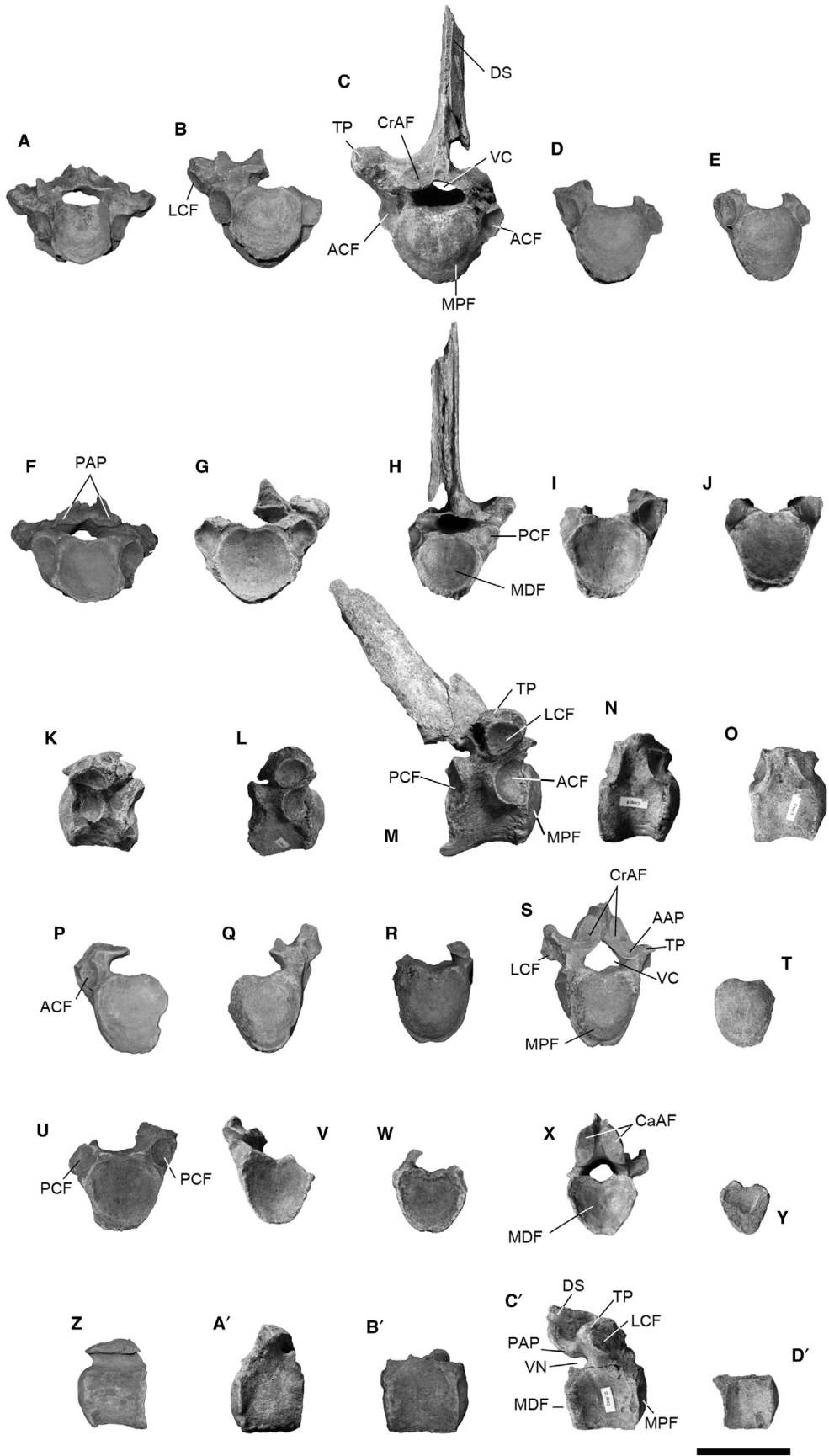


Fig. 3. Thoracic vertebrae. A. Cranial view of 3rd thoracic. B. Cranial view of 4th thoracic. C. Cranial view of 5th thoracic. D. Cranial view of 6th thoracic. E. Cranial view of 7th thoracic. F. Caudal view of 3rd thoracic. G. Caudal view of 4th thoracic. H. Caudal view of 5th thoracic. I. Caudal view of 6th thoracic. J. Caudal view of 7th thoracic. K. Left side view of 3rd thoracic. L. Right side view of 4th thoracic. M. Right side view of 5th thoracic. N. Right side view of 6th thoracic. O. Right side view of 7th thoracic. P. Cranial view of 9th thoracic. Q. Cranial view of 10th thoracic. R. Cranial view of 12th or 13th thoracic. S. Cranial view of 15th or 16th thoracic. T. Cranial view of 18th thoracic. U. Caudal view of 9th thoracic. V. Caudal view of 10th thoracic. W. Caudal view of 12th or 13th thoracic. X. Caudal view of 15th or 16th thoracic. Y. Caudal view of 18th thoracic. Z. Left side view of 9th thoracic. A'. Left side view of 10th thoracic. B'. Right side view of 12th or 13th thoracic. C'. Right side view of 15th or 16th thoracic. D'. Right side view of 18th thoracic. AAP= anterior articular process; ACF= anterior costal facet; CaAF= caudal articular facet; CrAF= cranial articular facet; DS= dorsal spine; LCF= lateral costal facet; MDF= main distal facet; MPF= main proximal facet; PAP= posterior articular process; PCF= posterior costal facet; TP= transverse process; VC= vertebral canal; VN= vertebral notch. Scale bar represents 10 cm.

Postcranial skeleton with strong long bones and stocky metapodes; limbs are graviportal.

**Specimen.** Vertebral column (four cervicals, nine thoracics, four lumbar, one sacral, two caudals and several fragments of dorsal spines and neural arches), ribs, one stylohyoideum, one scapula, two humeri, two ulnae, two radia, one lunate, one pisiform, one unciform, two scaphoids, one trapezoid, one McIV, right and left coxals, two femora, one tibia, one fibula, one patella, one astragalus, one calcaneus, one ectocuneiform, one navicular, one each of MtII, MtIII and MtIV, and four phalanges (Fig. S1).

**Locality.** Ondorkhaan City, Khenty Province, eastern Mongolia (47°19'33.57"N, 110°40'1.58"E).

**Measurements.** See Table S1.

**Vertebral column.** Twenty-four vertebrae were found, as well as several fragments of the dorsal spine and neural arches. The cranial facet and caudal facet of the vertebral body in all the cervical, thoracic and lumbar vertebrate are respectively convex and concave.

Four cervicals (3rd, 4th, 5th, 7th) are recovered (Fig. 2). The dorsal spine of the 3rd, 4th and 5th cervical is broken off. That of the 7th projects dorsally but its distal end is missing. In lateral view, the cranial articular processes of all cervicals are inclined craniodorsally. The caudal articular facets of the 3rd cervical project caudally, whereas those of the other cervicals tend to extend caudodorsally. The cranial and caudal articular facets of all cervicals are almost flat, and both facets are inclined medially in the craniocaudal view. The 3rd cervical has an elongated transverse process that projects laterally in the craniocaudal view and has a wing-like outline and a cranioventrally-inclined part in the lateral view. The main parts of the transverse process are missing in the 4th and 5th cervicals, but the preserved parts project laterally. The transverse processes of the 7th cervical are short and project lateroventrally. The transverse foramina of the 3rd and 5th cervicals are oval; only their medial margins are preserved in the 4th cervical and they are missing in the 7th. On the body of the 7th cervical, a pair of oval posterior costal facets is present on the lateral margins of the caudal facet. The vertebral canal of all the cervicals is almost the same size, with a semicircular lumen in the cranial view. The cranial facet of the vertebral body is oval in the 3rd, 4th and 5th cervicals, but circular in the 7th. The ventral crest of all

cervicals is moderately sharp and the ventral margin of the vertebral body is concave in lateral view.

Ten thoracic vertebrae (3rd, 4th, 5th, 6th, 7th, 9th, 10th, 12th or 13th, 15 or 16th and 18th) are recovered (Fig. 3). Most are missing their neural arches, and only the 5th retains the dorsal spine, which is long and inclined caudodorsally in the lateral view. The transverse process of all the thoracic vertebrae is massive and directs laterally. In the 3rd and 4th thoracic vertebrae, the lateral costal facets are large, deep and directed ventrolaterally whereas those of the 16th thoracic vertebra are small and shallow and face more cranio-laterally. In the cranial-side thoracic vertebrae, the cranial articular facets are almost flat and face dorsally while the caudal articular facet is also flat and faces ventrally. In contrast, those on the caudal side are similar to the lumbar vertebra in having concave, elliptical cranial articular facets that face dorsocranially and convex caudal articular facets that face caudoventrally. In the cranial-side thoracic vertebrae, the anterior and posterior costal facets are large and deep and are situated at midheight of the vertebral body. In contrast, in the caudal-side thoracic vertebrae, these facets tend to be small and shallow and are situated more dorsolaterally on the vertebral body. The vertebral canal is elliptical in the cranial-side thoracic vertebra, with a gradual change to sub-triangular in the caudal-side ones. In the cranial-side thoracic vertebrae, the cranial and caudal facets of the vertebral body both have a sub-circular outline, but in the caudal-side thoracic vertebrae, the outlines change to oval and heart-shaped, respectively. The ventral margin is concave in lateral view in the cranial-side thoracic vertebrae, but almost straight in the caudal-side thoracic vertebrae.

All lumbar vertebrae (the 1st, 2nd, 3rd and 4th) were collected, all missing the dorsal spine (Fig. 4A–K). The 1st to 3rd lumbar vertebrae are similar in form, but the 4th more closely resembles the sacral vertebra. In lateral view, the dorsal spine of the 1st to 3rd lumbar vertebrae is wide, being directed dorsally in the 1st and 2nd lumbar vertebrae and caudally in the 3rd. The lateral ends of the transverse process are missing in all the lumbar vertebrae, but the preserved parts show that the transverse process of the 1st and 2nd lumbar vertebrae are projected horizontally and are dorsoventrally flattened, while those of the 3rd and 4th lumbar vertebrae are more robust, with that of the 4th projecting slightly dorsally.

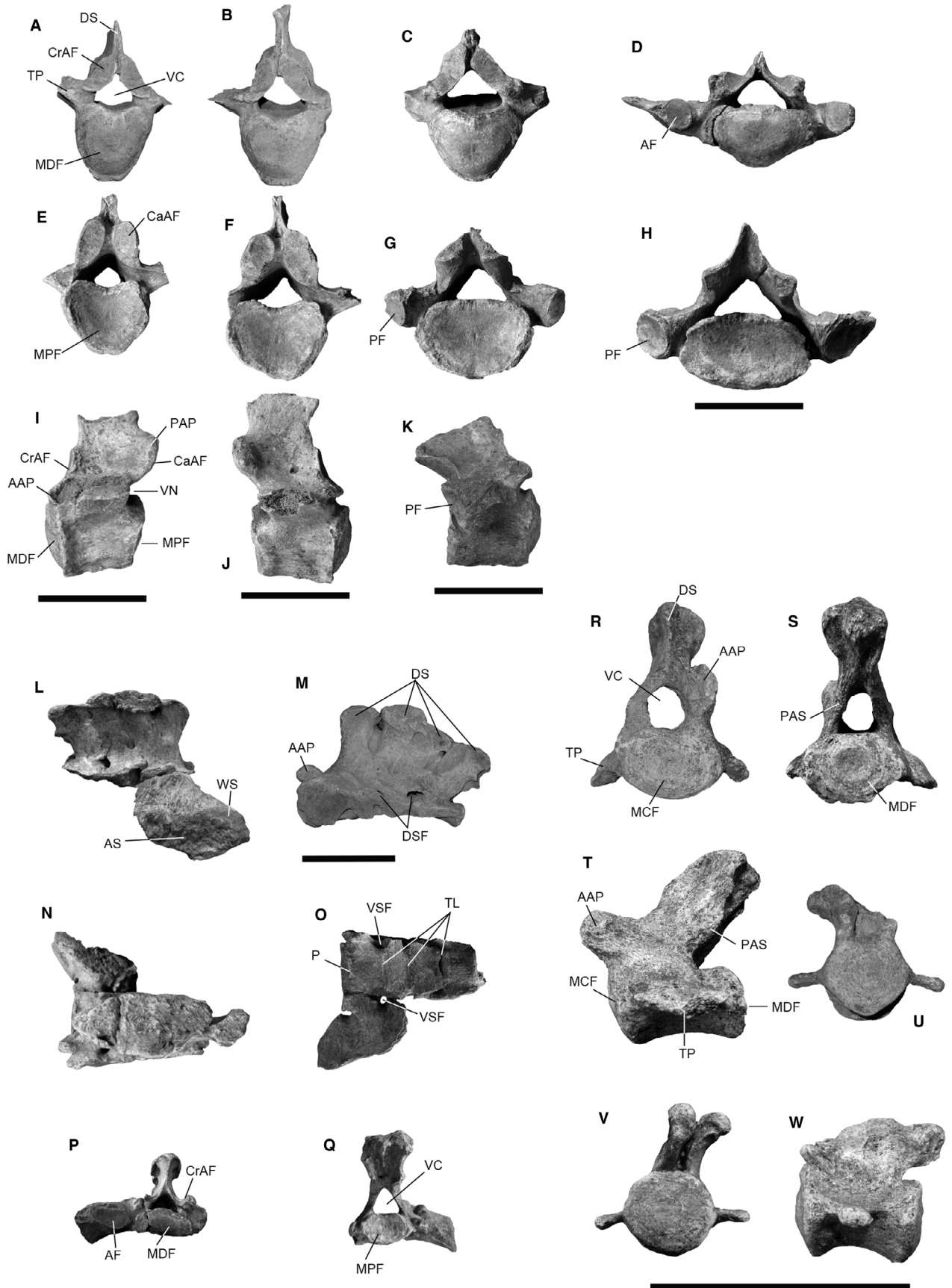


Fig. 4. Lumbar, sacrum and caudal vertebrae. A. Cranial view of 1st lumbar. B. Cranial view of 2nd lumbar. C. Cranial view of 3rd lumbar. D. Cranial view of 4th lumbar. E. Caudal view of 1st lumbar. F. Caudal view of 2nd lumbar. G. Caudal view of 3rd lumbar. H. Caudal view of 4th lumbar. I. Left side view of 1st lumbar. J. Right side view of 2nd lumbar. K. Right side view of 3rd lumbar. L. Right side view of sacrum. M. Left side view of sacrum. N. Dorsal view of sacrum. O. Ventral view of sacrum. P. Cranial view of sacrum. Q. Caudal view of sacrum. R. Cranial view of a larger sized caudal vertebra. S. Caudal view of vertebra in R. T. Left side view of vertebra in R. U. Cranial view of a smaller sized caudal vertebra. V. Caudal view of vertebra in U. W. Left side view of vertebra in U. AAP= anterior articular process; AF= anterior facet; AS= articular surface; CaAF= caudal articular facet; CrAF= cranial articular facet; DS= dorsal spine; DSF= dorsal sacral foramina; MCF= main cranial facet; MDF= main distal facet; MPF= main proximal facet; P= promontory; PAP= posterior articular process; PAS= posterior articular surface; PF= posterior facet; TL= transverse lines; TP= transverse process; VC= vertebral canal; VN= vertebral notch. VSF= ventral sacral foramina; WS= wing of sacrum. Scale bars represent 10 cm.

The vertebral canal of each lumbar vertebra is subtriangular in the craniocaudal view. In the 1st to 3rd lumbar vertebrae, the cranial articular facets have a concave surface and elongated-elliptical outline, but in the 4th lumbar these facets, while still concave, are much smaller and teardrop-shaped. The caudal articular processes extend caudally and have convex facets. The 3rd and 4th lumbar vertebrae have circular articular surfaces on the anterior and posterior sides of the transverse processes, respectively. The vertebral arch is high in cranial view in the 1st to 3rd lumbar vertebrae, and low in the 4th lumbar vertebra, but wide in the lateral view. The cranial and caudal facets of the vertebral body in the 1st and 2nd lumbar vertebrae are all heart-like in outlines, the 3rd lumbar vertebra has a heart-like cranial facet and an elliptical caudal facet, and both facets of the 4th lumbar vertebra have a dorsoventrally compressed elliptical outline. The ventral margin of the vertebral body is almost straight in the 1st to 3rd lumbar vertebrae.

The sacrum is composed of four fused vertebrae (Fig. 4L–Q), the dorsal spines of which project dorsally to dorsocaudally, each with a robust tip. The transverse processes of the 1st and 2nd sacral vertebrae are fused into a wing-like shape that forms the articular facet of the pelvis. The cranial articular facets are robust and project craniodorsally in the lateral view. The caudal articular facet is situated on the caudal margin of the dorsal spine of the last sacral vertebra along with small projections in the middle of the dorsal spine that also articulate to the 1st caudal vertebra. There is also an elliptical, cranially-facing, lateral articular facet for the last lumbar on each transverse process. The vertebral canals are triangular, smaller on the cranial side of the sacrum and much larger on the caudal side. The cranial and caudal facets of the sacrum are elliptical, although the cranial-side facet of the 1st sacral vertebra is much more compressed dorsoventrally than that of the 4th vertebra.

Two isolated caudal vertebrae were collected (Fig. 4R–W). Both are relatively small, suggesting that they are posterior-side ones. The proximal one is larger than the other (Fig. 4). Its transverse processes are tiny but the tips of both are broken. The cranial articular process is missing on the right side. The dorsal spine is short and inclines posteriorly in lateral view. The transverse processes project lateroventrally in the ante-

rior view. The vertebral arch is massive in the lateral view. The cranial articular process is tongue-shaped and projects anterodorsally in lateral view. There is a trace of the caudal articular processes on the posterior margin of the vertebral arch. The vertebral canal is oval. The vertebral body is cylindrical and longer than wide. Both cranial and caudal facets of the vertebral body are elliptical, the former being convex, the latter slightly concave. The other, smaller caudal vertebra has a deformed dorsal spine that is deeply inclined caudally, resulting in an uncertain outline of the vertebral canal (Fig. 4R–W). The cranial articular processes are shorter and smaller than those of the larger caudal, and there are no caudal articular processes. The transverse processes are thin and project laterally in the craniocaudal view. The vertebral body is cylindrical, with a concave ventral surface in the lateral view and nearly flat cranial and caudal facets that are pentagonal and circular in outline, respectively.

Ribs. At least 24 well-preserved ribs (Fig. S2) and several rib fragments were collected. The cranial-side ribs are missing their distal halves. The middle or distal parts of several ribs display cracks, possibly due to drying before they were buried. The cranial-side ribs are robust and wide in mediolateral view, while the caudal-side ribs are slender and thin and also more curved than the former. The heads of the cranial-side ribs are robust, but gradually become reduced posteriorly. A tubercle is developed on the cranial-side close to the head, but is reduced and situated farther away from the head, or is fully absent, in the caudal-side ribs. A costal groove is only developed on the cranial-side ribs. One left caudal-side rib has a swollen part distally, possibly the sign of a healed bone fracture.

Right stylohyoideum. The proximal end of this tiny, slender bone (Fig. 5A–B) is relatively wide and is divided into a dorsal process and the styloideus angle, the latter being slightly bent laterally. There is an articular facet for the ceratohyoid at the distal end, but none for the tympanohyoid.

Right scapula. The scapular body (Fig. 5C–E) has a long proximodistal axis, a gently concave posterior margin, a shallow scapular notch and a wide scapular neck; its dorsal and anterior margins are missing and the scapular spine is broken. Both the supraspinous and infraspinous fossae are almost flat, the coracoid process



Fig. 5. Stylohyoideum, scapula and humeri. A. Lateral view of stylohyoideum. B. Medial view of stylohyoideum. C. Lateral view of scapula. D. Medial view of scapula. E. Distal view of humeri. F. Cranial view of right humerus. G. Caudal view of right humerus. H. Cranial view of left humerus. I. Caudal view of left humerus. C = capitulum; Cp = coracoid process; Dt = deltoid tuberosity; Ec = epicondyle crest; FcCe = facet for ceratohyoid; Fs = facies serrata; Gf = glenoid fossa; H = head; Isf = infraspinous fossa; Le = lateral epicondyle; Lib = Lateral lip border; Ltc = lesser tubercle convexity; Me = medial epicondyle; Mlb = medial lip border; Mtm = *m. teres major* tuberosity; N = neck; Of = olecranon fossa; Pb = posterior border; Sa = styloideus angle; Sn = scapular notch; Ss = scapular spine; Ssf = supraspinous fossa; Suf = subscapular fossa; T = trochlea; Tg = trochlea groove. Scale bars represent 10 cm.

is round and knob-like, the *facies serrata* is rugose in medial view, the subscapular fossa is slightly concave and the glenoid fossa is oval.

**Humerus.** Both the right and left humeri were collected (Fig. 5F–I), minus their broken-off proximal parts. The preserved head of the right humerus is mediolaterally wide. The lesser tubercle is moderately swollen, the deltoid tuberosity is massive and the *m. teres major* tuberosity is almost flat and slightly rugose. The lateral epicondyle is larger than the medial one and is well expanded laterally. The epicondylar crest is sharp, the olecranon fossa is low and there is no distal gutter on the epicondyle. The distal articulation of the trochlea is mediolaterally compressed and diablo-shaped; the tro-

chlea groove is shallow and there is no scar on the trochlea.

**Radius.** Both right and left radii were collected (Fig. 6A–F). The proximal medial articular surface is larger than the lateral ones with an M-shaped anterior border. The radial tuberosity is prominent and the medial border of the diaphysis is concave. The lateral synovial articular surface is large with a triangular outline whereas the medial one is thin and shallow. The radius is in contact with the ulna and the proximal ulnar facet is fused. The insertion of *m. biceps brachii* is shallow and the gutter for *m. extensor carpi* is weakly developed. The interosseous crest is sharp and runs along the laterodistal margin of the shaft. There is no second distal



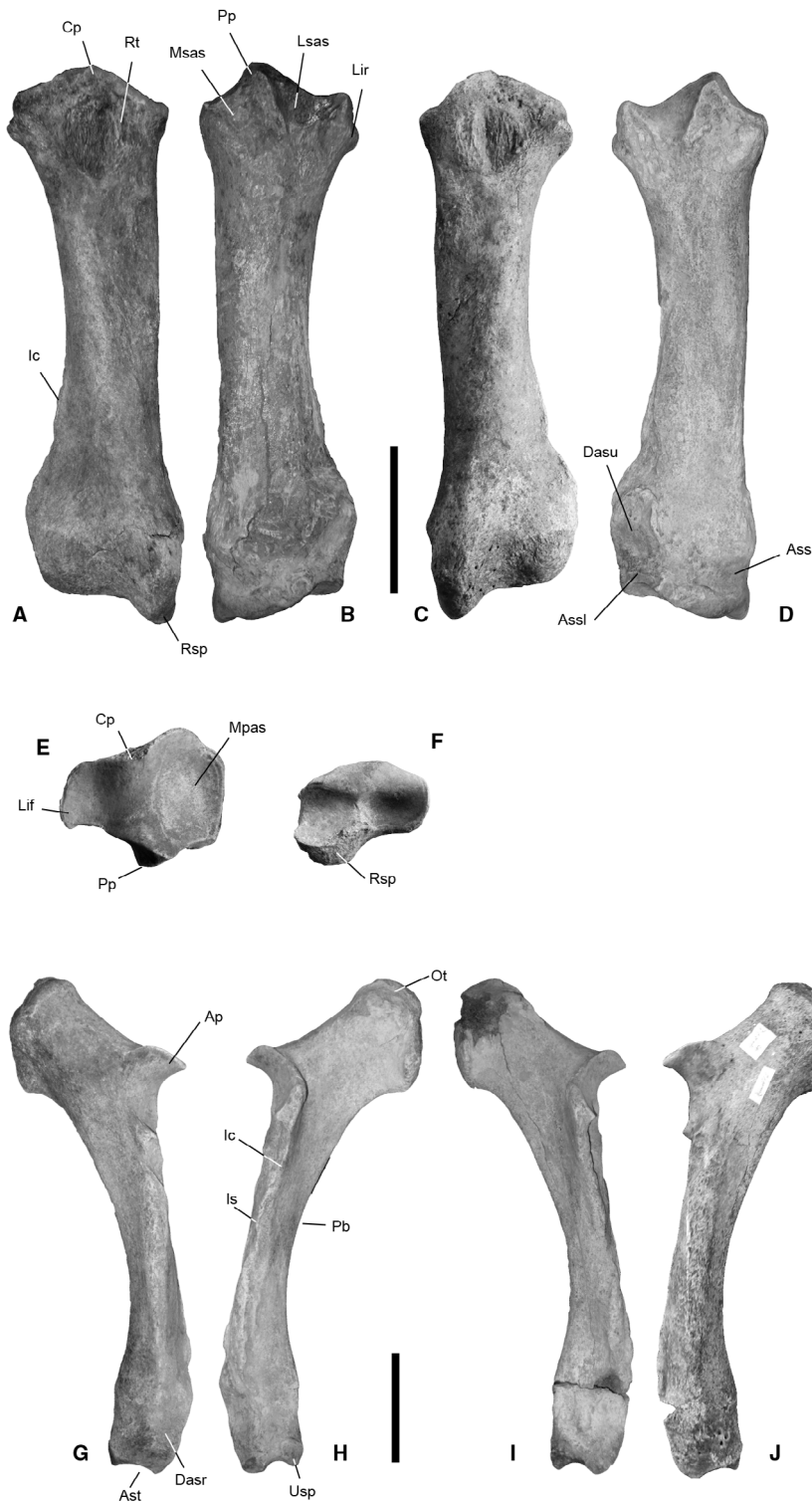


**Fig. 6.** Radii and ulnae. A. Cranial view of right radius. B. Caudal view of right radius. C. Cranial view of left radius. D. Caudal view of left radius. E. Proximal view of left radius. F. Distal view of the left radius. G. Lateral view of right ulna. H. Medial view of right ulna. I. Medial view of left ulna. J. Lateral view of left ulna. Ap=anconeal process; Ass=articular surface for scaphoid; Assl=articular surface for lunate; Ast=articular surface for the triquetrum; Cp=coronoid process; Dasr=distal articular surface for the radius; Dasu=distal articular surface of ulna; Ic=interosseous crest; Is=interosseous space; Lir=lateral insertion relief; Lsas=lateral synovial articular surface; Mpas=medial proximal articular surface; Msas=medial synovial articular surface; Ot=olecranon tuberosity; Pb=palmar border; Pp=palmar process; Rsp=radial styloid process; Rt=radial tuberosity; Usp=ulnar styloid process. Scale bars represent 10 cm.

facet for the ulna, and also no pyramidal facet. The posterior expansion of the scaphoid facet is high and the articular surface for the lunate is a trapezoidal shape. A radial styloid process is developed with an acute apex.

**Ulna.** Both the right and left ulnae were collected (Fig. 6G–J). The olecranon tuberosity is massive while the medial tuberosity of the olecranon is small. The angle between the diaphysis and olecranon is closed. An anconeal process is developed. The interosseous crest runs along to the proximal half of the shaft with the interosseous space. The shaft is nearly triangular in cross-section. The distal articular surface for the radius is broad, and the articular surface for the pyramidal is shallow-concave in the mediolateral view, but there is no anterior tubercle on the distal end is absent. An ulnar styloid process is developed, with an acute apex.

**Lunate.** One lunate was collected (Fig. 7A–C). In the dorsal view, the distal end of its dorsal side is rounded and the dorsal surface is smooth. A broad facet of the radius and a laterally adjacent, smaller facet for the ulna are both visible in dorsal view and situated dorsally in proximal view. In the lateromedial view, the facets for the magnum and unciform are deeply concave. There are three facets for the scaphoid on the medial side, with oval or hemispherical outlines. In the lateral view, two facets for the pyramidal are visible, a small, elongated facet

volar to the facet for the ulna, and another elongated facet adjacent to the unciform facet.

**Unciform.** One unciform was collected (Fig. 7D–E). This bone is mushroom-shaped in proximal view, trapezoidal in dorsal view. The volar process is long and appears distally bent in proximal view. There is no contact between the pyramidal and the McV facet, and no palmar expansion of the pyramidal facet is present.

**Scaphoid.** Both the right and left scaphoids were collected (Fig. 7K–N). In the dorsal view, this bone is almost rectangular and the dorsal surface is rugose. The posteroproximal lunate facet sits on a process, the radial facet is deeply saddle-shaped, the facet for the trapezoid is shallowly concave, the magnum facet is slightly concave in lateral view and a small, semicircular facet for the lunate is visible in volar view. The bone's height is identical at both its anterior and posterior ends.

**Trapezoid.** One trapezoid was collected (Fig. 7F–H). In the dorsal view, this bone is elliptical, although the proximal border appears dissymmetric. Both the scaphoidal and McII facets are deeply concave in the mediolateral view, while the facet for the magnum is smooth and flat.

**Pisiform.** One pisiform was collected (Fig. 7I–J). This bone is widest caudally and tapers toward the cranial side end. Both ends are thick in the dorsal view, and the caudal

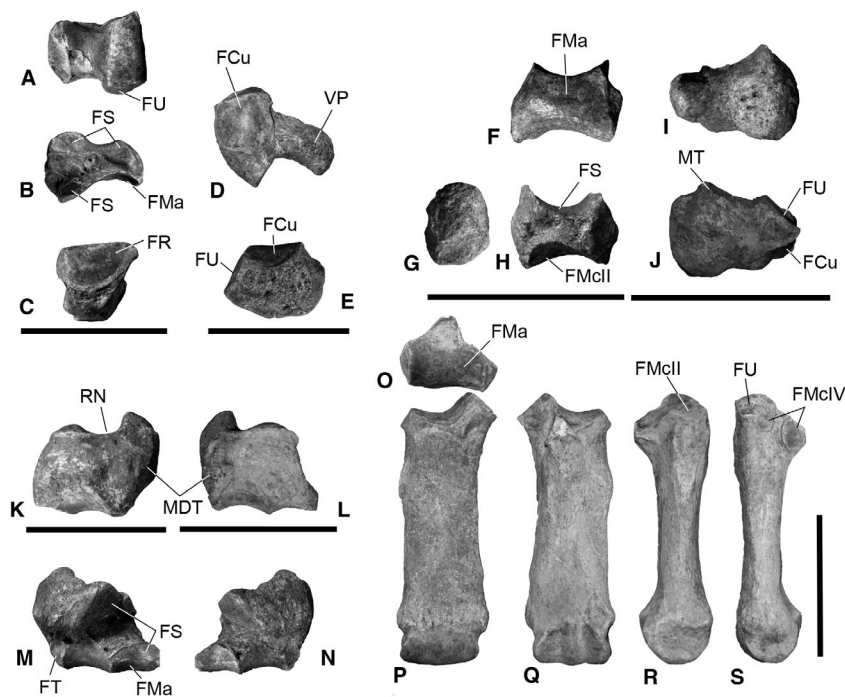


**Fig. 7.** Manus elements. A. Proximal view of lunate. B. Lateral view of lunate. C. Dorsal view of lunate. D. Cranial view of unciform. E. Dorsal view of unciform. F. Medial view of trapezoid. G. Dorsal view of trapezoid. H. Lateral view of trapezoid. I. Medial view of pisiform. J. Lateral view of pisiform. K. Dorsal view of right scaphoid. L. Dorsal view of left scaphoid. M. Palmar view of right scaphoid. N. Palmar view of left scaphoid. O. Proximal view of 3rd metatarsal. P. Dorsal view of 3rd metatarsal. Q. Palmar view of 3rd metatarsal. R. Medial view of 3rd metatarsal. S. Lateral view of 3rd metatarsal. FCu = facet for cuneiform; FMa = facet for magnum; FR = facet for radius; FS = facet for scaphoid; FT = facet for trapezoid; FU = facet for ulna; FMcII = facet for McII; FMcIV = facet for McIV; MDT = mediolateral tuberosity; MT = medial tuberosity; RN = radial notch; VP = volar process. Scale bars for A–N and O–S represent 5 and 10 cm, respectively.

end is robust and bent medially. The medial tubercle runs transversely. The cranial side is pointed in the lateral view. In the dorsal view, the facet for the lunate is semicircular; in dorsal view, the facet for the cuneiform is narrow.

**Metacarpal.** One McIII of slender proportions was collected (Fig. 7O–S). The insertion of the *m. expansor carpalis* is flat, that of the *m. interossei* is short, the intermediate relief is low and smooth, and there is no palmodistal tubercle on the diaphysis is absent. The shaft is straight proximodistally and flat on the dorsopalmarly. The proximal articular facet for the magnum is triangular and moderately concave. The two facets for the McIV are separated and are circular and sub-triangular, the facet for the McII is small and oval and the facet for the unciform is slightly convex.

**Coxal bone.** Both the right and left coxal bones were collected. The pubes are almost wholly broken away (Fig. 8), and the ischial ramus, ischial symphysis and distal part of both are missing. The iliac body is T-shaped in dorsal view, with a broken anterior margin and broken sacral tube. The gluteal surface is almost smooth. The greater ischiatic notch is deeply concave, the lesser ischiatic notch is shallow, the ischiatic spine is moderately

developed and the ischial arch curves dorsally. The psoas tub is rugose. The acetabulum is oval in shape and extremely deep and the acetabular fossa is remarkable. The lunate articular surface is smooth.

**Femur.** Both the right and left femora were found (Fig. 9). The proximal epiphysis is wide and the distal one is massive. The medial margin of the shaft is curved laterally in the dorsocaudal view. The femur head is hemispherical, the *fovea capitis* is high and narrow and the neck is robust. The greater trochanter is low and expanded laterodistally, while the lesser trochanter has a low and thin, ridge-like shape. The extremely well-developed third trochanter is curved proximodorsally. Both the medial and lateral epicondyles are massive. The angle between the medial rip and the diaphysis is steep. The medial and lateral trochanters are unequally high in the distal view, the proximal border of the patellar trochlea is curved, the medial and lateral trochanter ridges are not parallel, and the trochanter groove and intercondylar space appear deep in the distal view.

**Tibia.** The left tibia was collected (Fig. 10A–F). Its proximal and distal epiphyses are massive and the shaft is almost straight in the dorsocaudal view. The lateral intercondylar tubercle is higher than the medial one, the

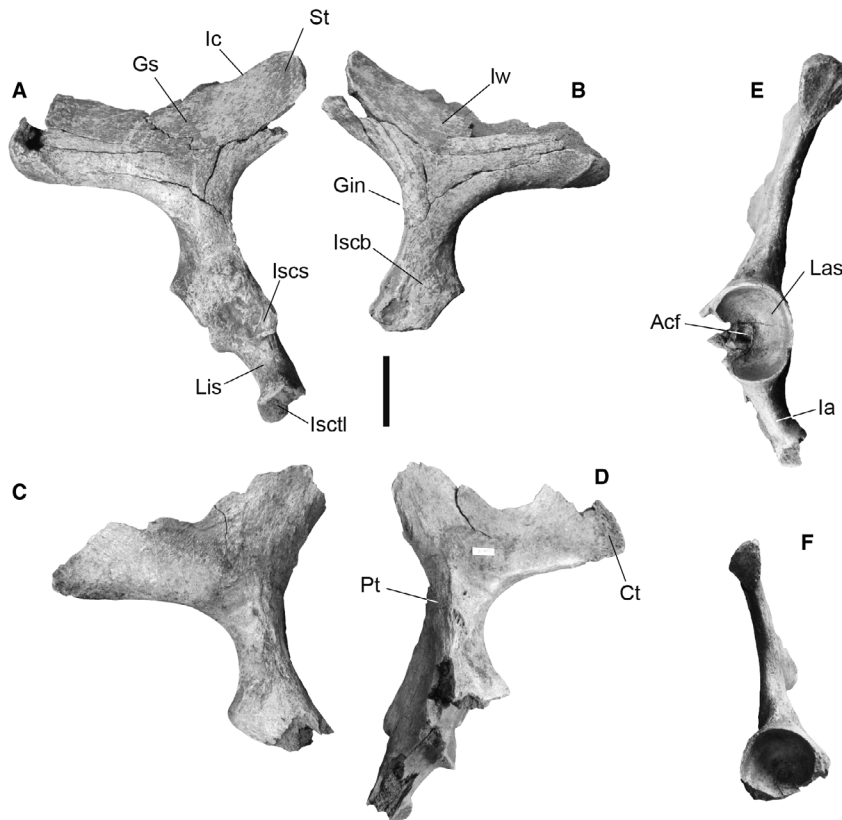
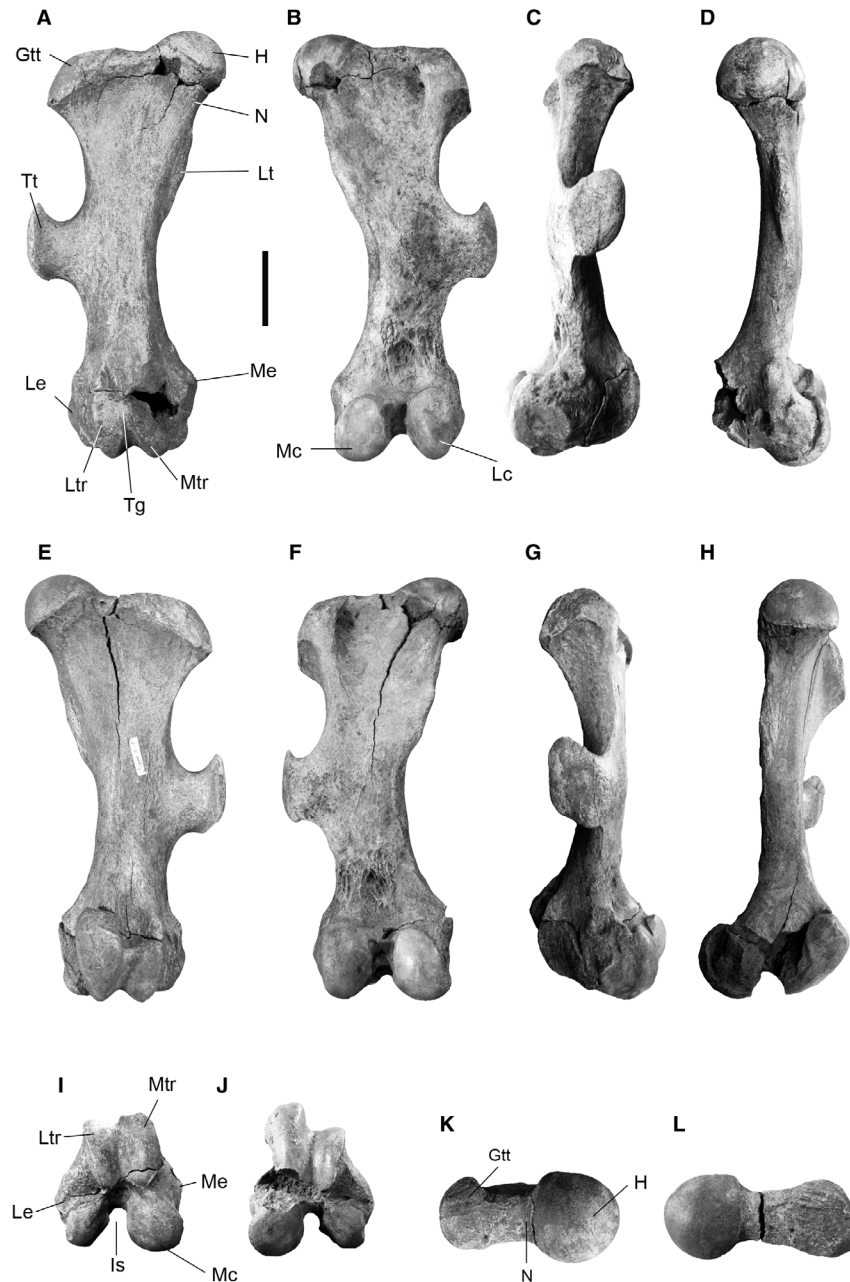


Fig. 8. Coxal bones. A. Dorsal view of left coxal bone. B. Dorsal view of right coxal bone. C. Ventral view of right coxal bone. D. Ventral view of left coxal bone. E. Lateral view of left coxal bone. F. Lateral view of right coxal bone. Ace = acetabulum; Acf = acetabular fossa; Ct = coxal tuber; Gin = greater ischiatic notch; Gs = gluteal surface; Ia = ischial arch; Ic = iliac crest; Iscb = ischiatic body; Iscs = ischiatic spine; Isctl = ischial tuber locks; Iw = iliac wing; Las = lunate articular surface; Lis = lesser ischial notch; Pt = psoas tub; St = sacral tuber. Scale bar represents 10 cm.



**Fig. 9.** Femora. A. Cranial view of right femur. B. Caudal view of right femur. C. Lateral view of right femur. D. Medial view of right femur. E. Cranial view of left femur. F. Caudal view of left femur. G. Lateral view of left femur. H. Medial view of left femur. I. Distal view of right femur. J. Distal view of left femur. K. Proximal view of right femur. L. Proximal view of left femur. Gtt = great trochanter top; H = head; Is = intercondylar space; Lc = lateral condyle; Le = lateral epicondyle; Lt = lesser trochanter; Ltr = lateral trochanter ridge; Mc = medial condyle; Me = medial epicondyle; Mtr = medial trochanter ridge; N = neck; Tg = trochanter groove; Tt = third trochanter. Scale bar represents 10 cm.

preserved part of the central intercondylar area is shallowly concave. The proximal medial articular surface is low, yet larger than the lateral one in the proximal view. The sliding surface for the *m. popliteus* is gently inclined caudally. The popliteal notch is a U-shape with an obtuse angle. The tibial tuberosity appears rounded in the proximal view. The extensor groove is shallow. The proximal articular surface is an isosceles triangle. The

tibial crest is blunt; it extends caudally and disappears in the middle part of the shaft. The distal articular surface for the fibula is triangular and it is reduced proximally. In the distal view, the distal articular surface for the astragalus is a rectangular shape. The medial groove is larger than the lateral one, there is no anterodorsal groove, the mediolateral gutter is shallow and the caudal apophysis is high and rounded.

**Fibula.** Only the proximal part of the left fibula was collected (Fig. 10G–J). The fibular head is gently curved laterally. The shaft is slender and straight distally. Its distal part is compressed mediolaterally. While the cranio-lateral line is sharp, the caudolateral line is more rounded. The proximal articular surface of the tibia is sub-triangular and rugose.

**Patella.** One patella was collected (Fig. 10K–L). It is massive and its dorsal surface is rugose. The apex of the patella and its cartilage processes are developed both distally and medially, making this bone sub-rhomboidal in outline. The base is concave and the facet for the trochlea is smooth with a vertical ridge.

**Calcaneus.** Only one calcaneus was collected, in perfectly preserved condition (Fig. 11A–C). Overall, it is short and robust, and its lateral surface is more rugose than the rest. A facet for the tibia is present, but no for the fibula. The *tuber calcanei* is well developed, being oval in proximal view and massive, and the insertion of *m. fibularis longus* is marked. One of the facets for the astragalus is slightly swollen while the other two are weakly concave, and the cuboid facet is small and concave.

**Right astragalus.** Only one astragalus was present (Fig. 11H–M). Its TD/H ratio is 1.16, and the APD/H ratio is 0.76. The fibula-facet is flat and orientated sub-vertically. The *column tali* is high. There is a posterior stop on the cuboid-facet. The caudal border of the trochlea is sinuous in the proximal view. The angle between the trochlea and the distal articulation is slightly oblique. The expansion of the facet 1 for the calcaneus is low and large. The facet 1 for the calcaneus in the lateral view is deeply concave. The facets 2 and 3 for the calcaneus are fused.

**Ectocuneiform.** Only one ectocuneiform was collected (Fig. 11D–E). Its outline in the proximodistal view is almost triangular. The articular facet for the navicular is weakly concave. In distal view, the articular facet for the MtIII is less concave than that for the navicular. The articular facets for the cuboid are oval and hemispherical. Of the three articular facets for the mesocuneiform, two are hemispherical and the other one is circular. The posterolateral process appears weak in proximal view.

**Navicular.** Only one navicular was collected (Fig. 11F–G). It is rectangular in proximal view, and its cross-section in lateral view is also rectangular. The articular facet for the astragalus is concave and its outline is almost rectangular. Three articular facets are visible in distal view, those for the ectocuneiform, mesocuneiform and entocuneiform. Of these, the oval facet for the entocuneiform is the smallest while the triangular facet for the ectocuneiform is largest, with the sub-triangular facet for the mesocuneiform being intermediate size. The articular facet for the cuboid is weakly concave.

**Metatarsal.** Three left metatarsals (MtII to MtIV) were collected (Fig. 11N–I). All are slender and, just as in the metacarpal described above, the insertion of the *m.*

*expansor carpalis* is flat, the intermediate relief is low and smooth and there is no palmodistal tubercle on the diaphysis.

MtII is well preserved (Fig. 11N–Q). Its body is bent medially. The proximal facet for the mesocuneiform is semicircular in shape and concave. In the medial view, two nearly circular facets for MtIII are visible, the dorsal one being larger than the palmar one. A small facet for the entocuneiform is present on the palmar side of the proximal end.

In MtIII there is no distal widening of the diaphysis (Fig. 11R–U), and the proximal border of the dorsal edge is concave. The palmar side of the MtII-facet is distinct. In proximal view the facet for the ectocuneiform is slightly concave and sub-triangular, the cuboid-facet adjacent to it is extremely small. There are sub-circular facets for the MtIV on the lateral side of the proximal end, as well as a tear-drop shaped facet for the MtII and a tiny facet for the ectocuneiform. The palmar side of the diaphysis is concave.

In MtIV the diaphysis is bent laterally and is asymmetrical in dorsopalmar view (Fig. 11W–A'). The facet for the cuboid is sub-circular with a convex medial margin. The palmoproximal tuberosity is pad-like and continuous in proximal view. Facets for the MtIII are visible in the medial view, a larger one is on the dorsal side.

**Phalanges.** The proximal phalanx of the left MtIII and the proximal middle, and distal phalanges of the left MtIV were collected (Fig. 11B'–I'). The proximal phalanx of the MtIII and MtIV are both stump-like in dorsopalmar view and have a rugose surface (Fig. 11B'–E'). The proximal facet for MtIII is deeply concave in the mediolateral view, whereas the distal facet for the middle phalanx is gently concave in dorsopalmar view, and the symmetrical insertions for MtIII are situated laterally. The middle phalanx of MtIV also has a stumped-like shape and has a deeply concave trochlea (Fig. 11F'–G'). The distal phalanx of MtIV is rectangular mediolaterally slender (Fig. 11H'–I'), with a smooth proximal facet for the middle phalanx and a low ridge for the articulation on the surface.

## Comparisons

Four Late Pleistocene rhinoceroses were known from northern Eurasia, namely *Elasmotherium sibiricum*, *Stephanorhinus hemitoechus*, *Stephanorhinus kirchbergensis* and *Coelodonta antiquitatis* (Guérin 1980; Tong 2012; Schvyreva 2016; Kirillova *et al.* 2017; Kosintsev *et al.* 2019).

### *Comparison with Elasmotherium sibiricum*

The postcranial elements of *E. sibiricum* are the largest size among the Pleistocene Eurasian rhinocerotid species (Tong *et al.* 2018). H.E.M 2012.24.1 is smaller than *E. sibiricum* (Schvyreva 2016; Tong *et al.* 2018), and the

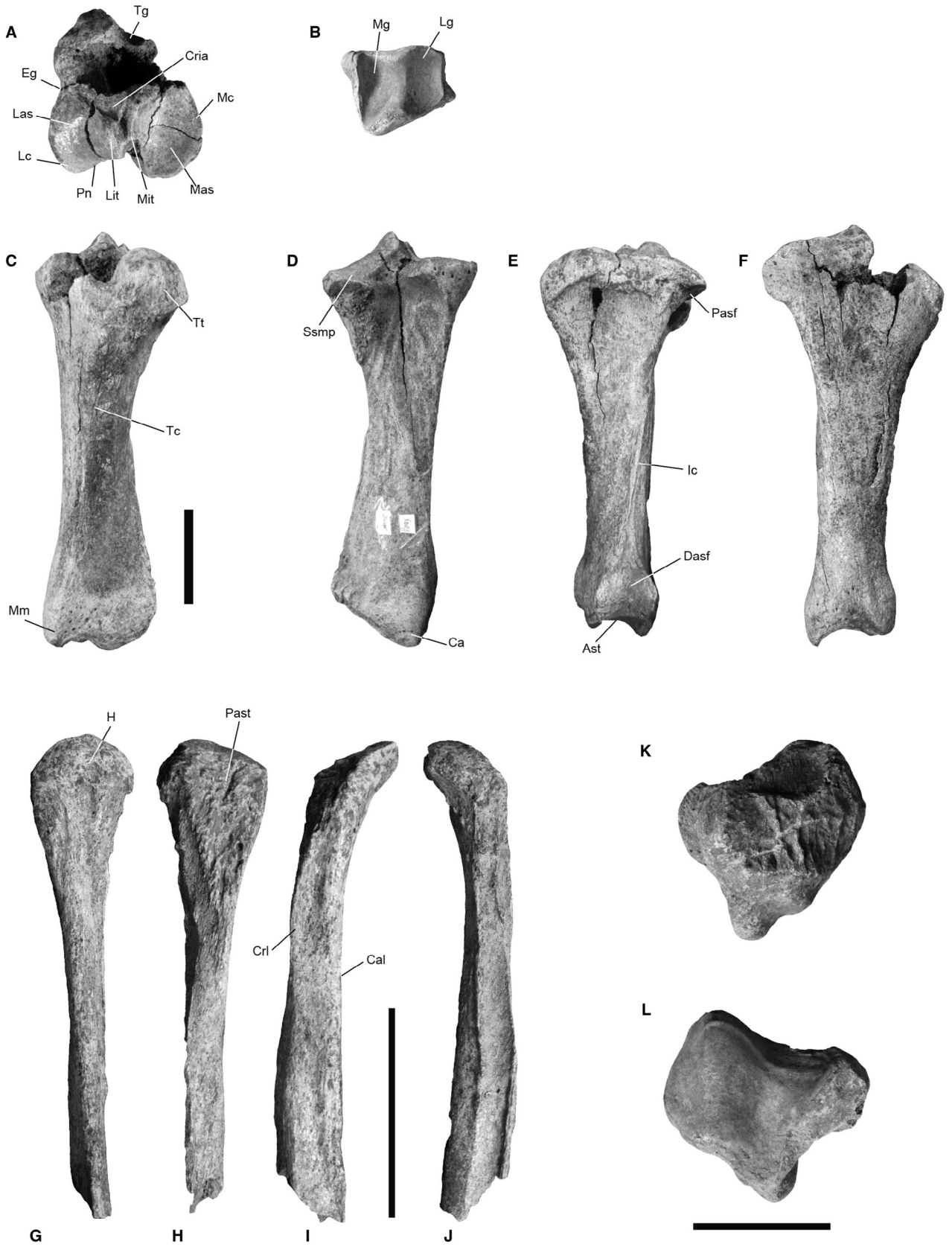


Fig. 10. Left tibia, fibula and patella. A. Proximal view of tibia. B. Distal view of tibia. C. Cranial view of tibia. D. Caudal view of tibia. E. Lateral view of tibia. F. Medial view of tibia. G. Lateral view of the left fibula. H. Medial view of the left fibula. I. Cranial view of the left fibula. J. Caudal view of the left fibula. K. Cranial view of patella. L. Caudal view of patella. Ast = articular surface for talus; Ca = caudal apophysis; Cal = caudal lateral line; Cri = cranial intercondylar area; Crl = cranial lateral line; Dasf = distal articular surface for fibula; Eg = extensor groove; H = head; Ic = iliac crest; Las = lateral articular surface; Lc = lateral condyle; Lg = lateral groove; Lit = lateral intercondylar tubercle; Mas = medial articular surface; Mc = medial condyle; Mg = medial groove; Mit = medial intercondylar tubercle; Mm = medial malleolus; Pasf = proximal articular surface for fibula; Past = proximal articular surface of tibia; Pn = popliteal notch; Ssmp = sliding surface for *m. popliteus*; Tc = interosseous crest; Tg = tuberosity groove; Tt = tibial tuberosity. Scale bars represent 10 cm.

size ranges of its bones are different (Fig. S3). The following comparison relies on Schvyreva's (2016) redescription of *E. sibiricum*. The radius of H.E.M 2012.24.1 has a more slender shaft and the radial styloid process is more acute. The shaft and the olecranon tuberosity of the ulna are more slender, the shaft is more gently curved, the anconeal process is better developed and the articular surface for the pyramidal is more concave. The radial notch of the scaphoid is more concave, the scaphoid's facet for the trapezium is more shallowly concave and the distal process on the trapezium facet is lower. On the lunate, the distal end of the cranial side is rounded, the cranial surface is smoother, the facet for the cuneiform is more elongated caudally, and the proximal side facets for the scaphoid are connected. On the pisiform, the medial tubercle is rounded and lower, the palmar side of the body is more robust and the facets for the lunate and cuneiform are not elongated caudally. Both the scaphoidal and McII facets of the trapezoid are more deeply concave in the medio-lateral view. The dorsal side of the unciform is more robust, and the volar process is more slender. The tibial shaft is more slender and the tibia's caudal apophysis is sharper. The calcaneus is more slender craniocaudally, the *tuber calcanei* is more massive, and also more robust in the caudal view, the insertion of *m. fibularis longus* is more concave and the facet for the cuboid faces more distomedially. On the astragalus, the orientation of the fibula facet is more inclined, the *column tali* is higher, the expansion of the facet 1 for the calcaneus is lower and larger, facet 2 is larger and fused with facet 3 and the medial tubercles less far distally. On the navicular, the facet for the astragalus is more shallowly concave, the cross-section in the lateral view is rectangular and the ectocuneiform has a nearly triangular outline.

#### *Comparison with Stephanorhinus kirchbergensis*

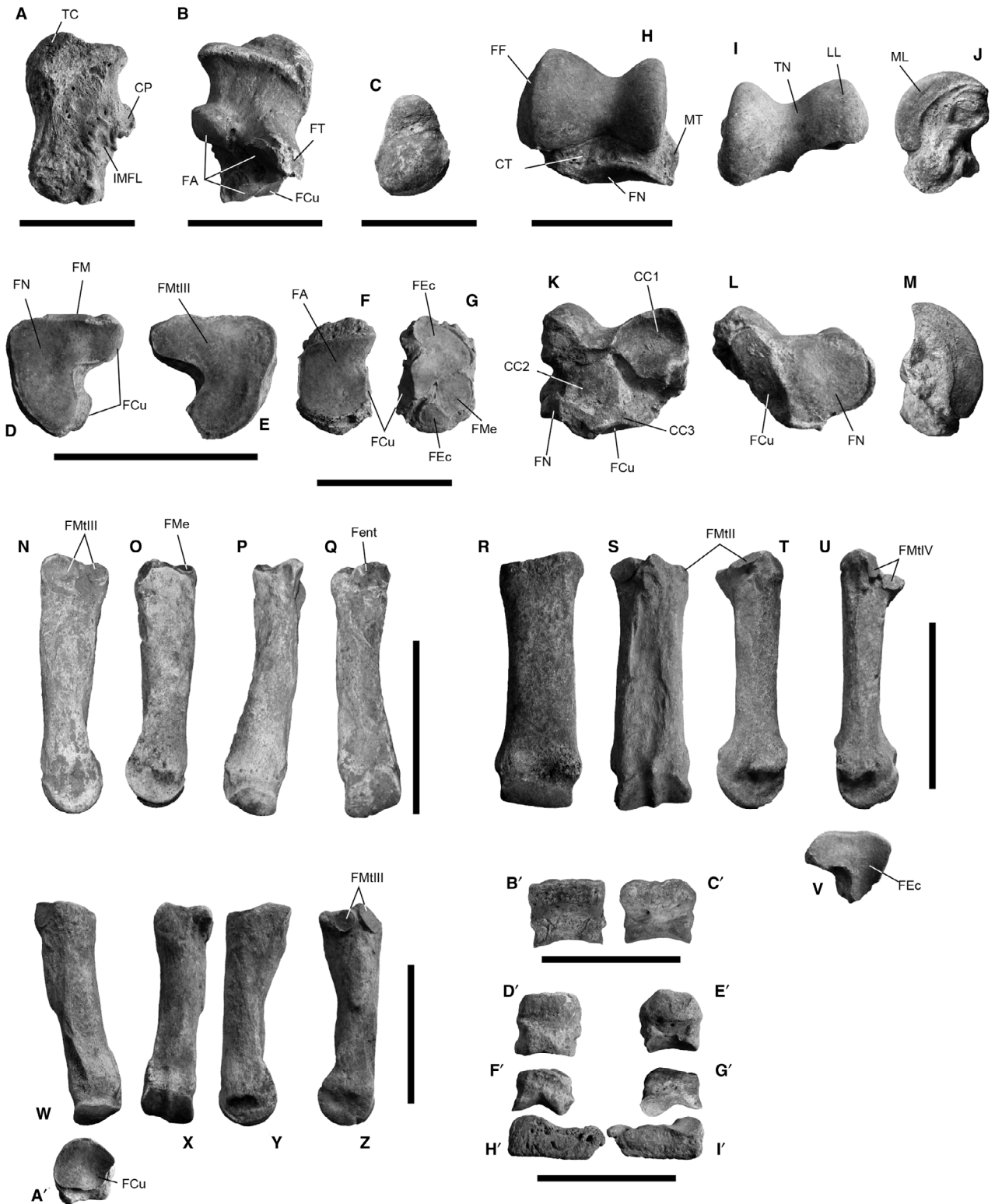
In terms of measurements, the compared elements of H.E.M 2012.24.1 differ significantly from those of *S. kirchbergensis* from all previously reported localities (Fig. S3).

Guérin (1973, 1980) described several Plio-Pleistocene rhinocerotids from western Europe, including *Stephanorhinus kirchbergensis* (as *Dicerorhinus mercki* in his paper). The postcrania of H.E.M 2012.24.1 differ in several ways from his descriptions. On the radius, the lateral margin is more rounded, the lateral proximal

articular surface is smaller, the medial proximal articular surface is wider and the radial styloid process is more robust. The unciform is proximodistally wider. The scaphoid has a greater posterior height and a better developed process of the posteroproximal lunate facet, and its trapezoid-facet is more clearly visible in the caudal view. The lunate has a smoother cranial surface and its facets for the cuneiform are more elongated. The trapezoid is proportionally much longer along its craniocaudal axis. The astragalus is much wider craniocaudally in lateral view, with a much larger expansion of the facet 1 for the calcaneus. The calcaneus has a much lower and wider *tuber calcanei*, a rounded coronoid process, and a marked insertion of *m. fibularis longus*. The navicular is wider in the cranio-caudal direction, with a more concave lateropalmar side of the proximal facet and a sub-circular facet for the mesocuneiform. The proximal end of MtII is much wider mediolaterally, with circular facets for MtIII. MtIV has a pad-shaped palmoproximal tuberosity and more circular outline of the facets for MtIII. On the other hand, there is similarity between H.E.M 2012.24.1 and *S. kirchbergensis* in the height of the medial and lateral trochanters and the rounded end of the medial trochanter in distal view of the femur, the width of MtIII and separated facets for MtIV on MtIII.

Kahlke (1977) described a specimen of *Dicerorhinus kirchbergensis* (= *S. kirchbergensis*) from Taubach in Germany. H.E.M 2012.24.1 differs from it in having a more robust coracoid process of the scapula, a more robust distal part of the humerus, and a projecting epicondylar crest. It also has a smaller lateral articular surface of the radius, a larger-sized lateral synovial articular surface and a more highly swollen radial styloid process. The present specimen's lunate has a more rounded distal corner in cranial view and a broader facet for the ulna in the lateral view, the pisiform has a better developed medial tubercle, the McIII has a more concave facet for the magnum and the tibia displays a more acutely angled caudal apophysis in the distal view. In addition, the astragalus has a larger lateral lip of the trochlea, the calcaneus has a less swollen *tuber calcanei*, the MtII has two facets for the MtIII those are separated and the MtIV has a more laterally bent shaft.

H.E.M 2012.24.1 differs from *S. kirchbergensis* of Fortelius *et al.* (1993) in having a more elliptical outline of the scapula's glenoid fossa, a more robust radial shaft, a more robustly proportioned scaphoid, a larger facet on the lunate for the magnum, a more robustly proportioned



but shorter McIII, a wider trochlea on the astragalus and a relatively greater craniopalmar width of the navicular.  
 H.E.M 2012.24.1 is distinguished from *S. kirchbergensis* from the Tomsk region of western Siberia

(Shpansky & Billia 2012) in having a more massive McIII and a proximodistally shorter astragalus, and its femur differs from that of *S. kirchbergensis* from the Middle Pleistocene locality in Nihewan Basin in China



Fig. 11. Pes elements. A. Lateral view of right calcaneus. B. Medial view of right calcaneus. C. Proximal view of right calcaneus. D. Proximal view of ectocuneiform. E. Distal view of ectocuneiform. F. Proximal view of navicular. G. Distal view of navicular. H. Cranial view of right astragalus. I. Proximal view of right astragalus. J. Medial view of right astragalus. K. Caudal view of right astragalus. L. Distal view of right astragalus. M. Lateral view of right astragalus. N. Medial view of left MtII. O. Lateral view of MtII. P. Dorsal view of left MtII. Q. Palmar view of left MtII. R. Dorsal view of MtIII. S. Palmar view of MtIII. T. Medial view of MtIII. U. Lateral view of MtIII. V. Proximal view of MtIII. W. Dorsal view of MtIV. X. Palmar view of MtIV. Y. Lateral view of MtIV. Z. Medial view of MtIV. A'. Proximal view of MtIV. B'. Dorsal view of the basal phalanx of MtIII. C'. Palmar view of the basal phalanx of MtIII. D'. Dorsal view of the basal phalanx of MtIV. E'. Palmar view of the basal phalanx of MtIV. F'. Dorsal view of the middle phalanx of MtIV. G'. Palmar view of the middle phalanx of MtIV. H'. Dorsal view of the distal phalanx of MtIV. I'. Palmar view of the distal phalanx of MtIV. CC1 = facet 1 for calcaneus; CC2 = facet 2 for calcaneus; CC3 = facet 3 for calcaneus; CP = coronoid process; CT = *columnnitali*; FA = facet for astragalus; FCu = facet for cuboid; FEc = facet for ectocuneiform; Fent = facet for entocuneiform; FF = facet for fibula; FM = facet for magnum; FMe = facet for mesocuneiform; FMtII = facet for MtII; FMtIII = facet for MtIII; FMtIV = facet for MtIV; FN = facet for navicular; FT = facet for tibia; IMFL = insertion of *m. fibularis longus*; LL = lateral lip; ML = medial lip; MT = medial tubercle; TC = tuber calcanei; TN = trochlea notch. Scale bars for A–A' and B'–I' represent 10 and 5 cm, respectively.

(Tong *et al.* 2014) in being more robustly proportioned with a more projecting third trochanter.

Lobachev *et al.* (2021) described *S. kirchbergensis* from Siberia. H.E.M 2012.24.1 differs from the Siberian remains in having more robust (radius, tibia and metapodial bones), asymmetrical outline of the proximal articular surface of the radius, radial styloid process of the radius in distal view, dorsocaudally wider at the proximal and distal ends of the radius, rectangular shaped navicular in dorsal view, lower height of the astragalus, and circular shaped facet for the cuboid on MtIV.

#### *Comparison with Stephanorhinus hemitoechus*

Compared with *S. hemitoechus* following Guérin (1973, 1980), H.E.M 2012.24.1 differs in having a radius with a more oval medial proximal articular surface and a more rugose and better developed radial tuberosity, a taller scaphoid, a mesiolaterally much broader unciform and an astragalus with a wider mediolaterally wider trochlea and a more projecting medial tubercle. It also has a lower angle between the trochlea and the distal articulation, a more robustly proportioned calcaneus, a navicular with a circular facet for the mesocuneiform, and a more circular proximal facet of the MtIV.

Fortelius *et al.* (1993) made a comparative description of the species of *Stephanorhinus*. H.E.M 2012.24.1 differs from their material of *S. hemitoechus* in having a more projecting radial styloid process and a lunate with a wider proximal side in proximal view, a smoother cranial surface and a more rounded distal margin in proximal view. It also has a more slender tibial shaft and a more acute angle at the caudomedial corner of the distal end; an astragalus with a higher angle between the trochlea and the distal articulation, a navicular that is more compressed mediolaterally, a broader proximal facet on the MtII in the proximal view and a more circular proximal facet on the MtIV in the proximal view.

H.E.M 2012.24.1 differs from *S. hemitoechus* following van der Made (2010) in having a more concave medial margin of the glenoid fossa of scapula, and on the radius, a more robust diaphysis, a smaller lateral articular surface and more swollen radial styloid process. Addi-

tionally, the navicular has a convex palmar margin and a circular facet for the mesocuneiform, while its scaphoid has a smaller facet for the lunate. Its MtII has a larger cranial-side facet for the MtIII, a more robust MtIII, with a more gently curved cranial margin of the proximal facet, and a more circular-shaped proximal facet on the MtIV.

H.E.M 2012.24.1 differs from remains referable to *S. hemitoechus* from Apulia in Italy (Pandolfi & Petronio 2011) in having a more oval shaped glenoid fossa of the scapula, a more robustly proportioned humerus with a narrow, oval olecranon fossa, a more massively proportioned tibia with a more acute caudal apophysis and a trapezoidal distal part in distal view, a more massive calcaneus, a lower astragalus, projected medial tubercle and dorsopalmarly narrow distal articular surface, and a more slender MtII.

Pandolfi & Tagliacozzo (2015) described *S. hemitoechus* from the Late Pleistocene locality of Valle Radice (Sora, central Italy). H.E.M 2012.24.1 different from *S. hemitoechus* by Pandolfi & Tagliacozzo (2015) in having a more robust shaft of the humerus, a prominent radial styloid process of the radius in distal view, a transversely wider facet for the magnum on the scaphoid, a rounded distal corner of the lunate, a dorsopalmarly wide trapezoid, robust proportions of the McIII, lower height of the astragalus, massive proportions of the calcaneus, robust proportions of the MtIII, and a circular shaped facet for the cuboid on the MtIV.

Compared with the Italian material, H.E.M 2012.24.1 has a similarly sized McIII and astragalus but a larger radius and a much more slender MtIII (Fig. S3).

#### *Comparison with Coelodonta antiquitatis*

Many parts of the postcrania of H.E.M 2012.24.1 resemble in postcrania described by Guérin (1973, 1980) from La Fage in France. Both have a radius with a prominent radial styloid process, a large and triangular lateral synovial articular surface and a shallow insertion of *m. biceps brachii*. The proportions of the unciform are also similar in distal view, and the McIII of both has a triangular proximal articular facet for the magnum, an oval facet for the McII and two facets for the MtIV that

were separated, with the cranial facet being circular and situated proximally. In both the astragalus has a sub-vertically-orientated and flattened fibula-facet, a high *column tali*, a slightly oblique angle between the trochlea and the distal articulation and a large, low expansion of calcaneus-facet 1. Similarity is also found in the fused calcaneum-facets 2 and 3, the MtII's semicircular proximal facet for the mesocuneiform, the MtIII's sub-triangular shaped facet for the ectocuneiform with a small, adjacent cuboid-facet, two separate facets for the MtIV with the lateral one situated on the proximal side, the scaphoid with an almost rectangular shaped outline in the cranial view, developed process of the scaphoid with the postero-proximal lunate facet, and the lunate with a rounded distal end in the cranial view. Additionally, there is a smooth cranial surface on the lunate, visible facets for the radius and ulna in the cranial view, an ectocuneiform with one circular facet and two hemispheres for the mesocuneiform and a weak postero-lateral process in the proximal view, and an MtIV with a pad-shaped palmoproximal tuberosity in the proximal view.

Differences between H.E.M 2012.24.1 and *C. antiquitatis* from La Fage in France by Guérin (1980) are also evident. In H.E.M 2012.24.1, the scapula has a more oval glenoid fossa in distal view and the radius has a much wider medial proximal articular surface and a much deeper gutter for the *m. extensor carpi*. The more robustly-shaped navicular has a less projecting cranio-medial corner and a semicircular facet for the mesocuneiform. The differences also include a mediolaterally narrower unciform in H.E.M 2012.24.1, a much wider trochlea of the astragalus as seen in medial view, a calcaneus that appears more robust in lateral view, a more robust *tuber calcanei*, a better developed insertion of *m. fibularis longus* on the calcaneus, the MtII's smaller caudal side facet for the MtIII, the scaphoid's wider facet for the trapezium and a more projecting craniodistal process, the MtIV's more semicircular proximal cuboid-facet and the trapezoid's more concave facets for the scaphoid and McII.

Borsuk-Bialyncka (1973) reported abundant remains of *C. antiquitatis* from Poland, the USSR and Czechoslovakia at that time. Compared with those remains, H.E.M 2012.24.1 has a similar humerus with a massive deltoid tuberosity, an almost flat *m. teres* major tuberosity, a sharp epicondylar crest, a low olecranon fossa, a diablo-shaped and mediolaterally compressed distal articulation of the trochlea, and also a similar radius with a well-developed radial tuberosity, concave medial border of the diaphysis, a triangular lateral synovial articular surface, a shallow insertion of *m. biceps brachii*, a sharp interosseous crest that runs along to the laterodistal margin of the shaft and a projecting radial styloid process with an acute apex. The similarity extends to the pisiform's acute medial tubercle, the unciform with trapezoid shaped outline in the cranial view, more bent

palmar process in the proximal view, the lunate with the broad facet for the radius on the dorsal side and smaller facet for the ulna in the cranial view, concave facets for the magnum and unciform of the lunate, the smooth anterior (cranial) surface of the lunate, and rounded distal end of the lunate in the cranial view. The scaphoid is also similar in the deep saddle-shaped radial facet, shallowly concave facet for the trapezoid, slightly concave facet for the magnum in the lateral view, the almost identical heights of the anterior and posterior parts, the McIII with the straight and flat diaphysis, and the two facets for the Mt IV that are separated. Of these, palmar one is a circular shaped. Additionally, there are similarities in the coxal bone with an almost smooth gluteal surface, deep concaved greater ischiatic notch, developed ischiatic spine and shallow lesser ischial notch, femur with massive proportions compared with other rhinocerotine species, the astragalus with high *column tali*, low and large expansion of the facet 1 for the calcaneus, and fusion of the facets 2 and 3 for the calcaneus. However, the H.E.M 2012.24.1 specimen differs in having a scapula with a more robust coracoid process, much taller proportions of the scaphoid, developed process of the scaphoid the postero-proximal lunate facet, and more slender tibia.

The H.E.M 2012.24.1 specimen is similar to *C. antiquitatis* from the Weser near Petershagen in northwest Germany (Diedrich 2008) in having a slender stylohyoideum, a robust radius with a radial styloid process, the ulna with a massive olecranon tuberosity, projecting anconeal process and distinctive interosseous space, robust metacarpal, massive proximal and distal parts of the femur along with a third trochanter, and a mediolaterally wide and proximodistally low astragalus with a projecting medial tubercle. However, it differs in having a tibia with a much more slender shaft and shallower tuberosity groove, and much more slender metatarsal.

H.E.M 2012.24.1 is similar to *C. antiquitatis* from Los Rosales and El Toll in Spain (Álvarez-Lao & García 2011) in having a projecting radial styloid process and separate facets for McIV on the McIII. On the other hand, the radius of H.E.M 2012.24.1 is much more robust than that of *C. antiquitatis* from Spain.

Pleistocene deposits in China have yielded many remains of *C. antiquitatis*, especially northeast and northern areas of the country (e.g. Tong & Moigne 2000). Based on these remains, radiocarbon dating and phylogenetic analyses have been done, and the palaeobiogeography has been discussed (e.g. Shuang *et al.* 2012; Stuart & Lister 2012), but most papers have described the crania, mandibles and cheek teeth of the Chinese specimens, with only poor, non-detailed descriptions of the postcrania. Therefore, comparison between H.E.M 2012.24.1 and *C. antiquitatis* from China must await more detailed descriptions of the latter.

In conclusion, H.E.M 2012.24.1 is clearly distinguished from *E. sibiricum* by its smaller size and much

more slender long bones. As for the other three candidate species, H.E.M 2012.24.1 exhibits certain unique features of *C. antiquitatis* such as a projecting radial styloid process and a shallowly concave distal end margin of the radius in the cranial view, and a lunate with rounded distal corner and a smooth anterior (cranial) surface in the cranial view (Fig. S4).

#### *AMS $^{14}\text{C}$ dates and $\delta^{13}\text{C}$ of woolly rhinoceros from Ondorkhaan*

The two  $^{14}\text{C}$  dates from H.E.M 2012.24.1 and the calibrated dates at  $2\sigma$  range are listed in Table 1. The calibrated dates of the two specimens are tightly spaced: 42 160–40 040 cal. a BP for ODK01 (UCIAMS-143223), and 42 105–39 955 cal. a BP for ODK02 (UCIAMS-143224), with  $\delta^{13}\text{C}$  values of  $-19.5\text{‰}$  for ODK01, and  $-20.2\text{‰}$  for ODK02.

#### Discussion

Based on comparisons with published data on Late Pleistocene rhinocerotids, we conclude that H.E.M 2012.24.1 belongs to *Coelodonta antiquitatis*. Although Kahlke & Lacombe (2008) discussed the morphological variations exhibited by woolly rhinoceros skulls and cheek teeth during the Middle to Late Pleistocene, data on the morphological variation of the postcrania of *C. antiquitatis* have been scarce. Guérin (1980) summarized the morphological variation of limb bones based on finds from western Europe and concluded that these limb bones tend to be more robust in younger strata (zone 24 (438–431 ka) to zone 26 (the entire Late Pleistocene)). Guérin (1980) also investigated metrical differences between specimens of *C. antiquitatis* from western Europe and China. He found no significant differences for the carpal and tarsal bones, but the long bones of Chinese specimens tended to be somewhat more slender than those of western European specimens.

Most measurements of the skeletal elements of H.E.M 2012.24.1 fall within the size ranges of western European materials published by Guérin (1980) (Fig. S3, Table S1). The differences in several characteristics of the postcrania from the limited number of adequately measured specimens of Eurasian woolly rhinoceros might reflect intraspecific variation, but additional remains from Mongolia are required to confirm this.

Size differences in skulls and postcrania have been interpreted by biometric means as evidence for sexual dimorphism in other rhinocerotids (e.g. Loose 1975; Groves 1982; Mead 2000; Mihlbachler 2007; Chen *et al.* 2010; Lu *et al.* 2020; Pandolfi *et al.* 2021), but compared to other rhinocerotids little is known about the sexual dimorphism of postcrania in the woolly rhinoceros. This subject cannot be usefully discussed until more description and measurement of postcranial elements of this species become available.

One of the left caudal side ribs in H.E.M 2012.24.1 shows signs of a healed bone fracture (Fig. S2). Diedrich (2008) reported a healing fractured rib of a woolly rhinoceros from Petershagen in Germany. He suggested that the fracture could have been caused by a strong blow to the side of the body during the individual's lifetime, perhaps the result of an intraspecific fight such as occur today in African rhinocerotid species. The rib fracture of H.E.M 2012.24.1 may have had the same cause.

The range of the woolly rhinoceros expanded southwards into the Iberian Peninsula (to about  $36^{\circ}\text{N}$ ) during MIS 3 and MIS 2, especially the former, nearly contemporaneously with (or at least corresponding to) Heinrich event 4 (H4: *c.* 41–36 ka: Álvarez-Lao & García 2011). According to Stuart & Lister (2012), the AMS radiocarbon dates of woolly rhinoceroses from south Siberia, Baikal region and East Asia mostly fall in the cold period between H5 and H4. The present study confirms that the Mammoth Faunas was distributed in eastern Mongolia during the cold period *c.* 45–40 ka. The narrow potential age range for H.E.M 2012.24.1, 41 100–41 030 cal. a BP using the medians of calibrated AMS  $^{14}\text{C}$  dates, tends to confirm our inference that the fossil bone samples from H.E.M 2012.24.1 are all from the same individual. This date range falls within the period of climatic amelioration that occurred between H5 (46 000 cal. a BP) and H4 (39 000 cal. a BP) (Hemming 2003).

The  $\delta^{13}\text{C}$  values of  $-19.5$  and  $-20.2\text{‰}$  for two rib samples taken from H.E.M 2012.24.1 are essentially identical to others reported for woolly rhinoceros in the mammoth steppe (max. =  $-17.3\text{‰}$ , min. =  $-21.1\text{‰}$ , median =  $-20.3\text{‰}$ ; Schwartz-Narbonne *et al.* 2019). They distinctly differ, however, from the  $\delta^{13}\text{C}$  values reported by Schwartz-Narbonne *et al.* (2019) for other mammals in southern Siberia during the Late Pleistocene (max. =  $-17.3\text{‰}$ , min. =  $-20.8\text{‰}$ , median =  $-18.6\text{‰}$ ) and for palaeosol layers formed during MIS 3 in the Baikal region (max. =  $-22.2\text{‰}$ , min. =  $-24.47\text{‰}$ , median =  $-22.6\text{‰}$ ). These differences suggest that either the woolly rhinoceros enjoyed a unique niche partitioning from other herbivores or the composition of the vegetation in northeastern Mongolia at the edge of the mammoth steppe was slightly different from that in other regions inhabited by the Mammoth Faunas.

#### Conclusions

In this paper, we described a rhinocerotid skeleton from Ondorkhaan, eastern Mongolia, and compared it with four Late Pleistocene rhinoceros species of northern Eurasia, identifying it as *Coelodonta antiquitatis*. AMS  $^{14}\text{C}$  dates obtained from two rib bones falling within the interval of 41 100–41 030 cal. a BP suggest that *C. antiquitatis* was distributed in eastern Mongolia *c.* 45–40 ka during the period of climatic amelioration between Heinrich events 5 and 4 as a member of the Mammoth

Faunas. The distribution of the  $\delta^{13}\text{C}$  values suggests that either the woolly rhinoceros enjoyed a unique niche partitioning from other herbivores, or the composition of the vegetation in northeastern Mongolia at the edge of the mammoth steppe was slightly different from that in other regions inhabited by the Mammoth Faunas.

Our findings from Mongolia are likely consistent with a recent argument on the evolutionary ecological context of woolly rhinoceros, i.e. the possibility of the niche partitioning of woolly rhinoceros separating it from those of both horse and woolly mammoth (Rey-Iglesia et al. 2021). Yet undescribed remains of woolly rhinoceros have been found at several localities in Mongolia, e.g. Norovlin, Altanbulag, Nalaikha (M. Izuho, pers. comm. 2021) and Salkhit (Tseveendorj et al. 2006). Accumulation of detailed studies of these specimens and further studies of their niches in Mongolia may greatly improve our understanding of the evolutionarily ecology of woolly rhinoceros in the context of the Mammoth Faunas, and may elucidate its relationship to the dispersal and adaptation of modern humans in northeast Asia.

*Acknowledgements.* – S. Yi (Seoul National University) kindly shared the news that the present specimen had been discovered in Ondorkhaan. We thank N. Nyamsuren, E. Sainzaya and B. Erdenesuvd (Ondorkhaan Local Museum) for obtaining permission to study the specimens and for providing logistic support. The UCIAMS dating reported here was done under the supervision of Dr T. Stafford, Jr., and the measurements were done at the University of California-Irvine AMS facility, under the direction of Dr J. Southon. We thank the editor-in-chief Jan A. Piotrowski and three anonymous reviewers who provided suggestions and constructive criticisms, greatly improving our manuscript. The authors also thank M. J. Grygier (National Museum of Marine Biology & Aquarium, Taiwan) for the correction of the English, which increased the quality of our manuscript. This research was made possible with support from the Heiwa Nakajima Foundation (PI: M. Izuho), and the Japan Society for Promotion of Science (JSPS) (grant 24320157, PI: M. Izuho; grant 26292087, PI: H. Takahara) and a Grant in-Aid for Scientific Research on Innovative Areas (Grant No. 1802 for FY2016-2020) from the Ministry of Education, Culture, Sports, Science and Technology, Japan ('Cultural history of PaleoAsia: Integrative research on the formative processes of modern human cultures in Asia', directed by Y. Nishiaki).

*Author contributions.* – NH, MI, KT and FI participated in writing of the manuscript. BT, BG, DO and LI participated in excavation, cleaning and repairing of the studied material.

## References

- Álvarez-Lao, D. J. & García, N. 2011: Southern dispersal and palaeoecological implications of woolly rhinoceros (*Coelodonta antiquitatis*): review of the Iberian occurrences. *Quaternary Science Reviews* 30, 2002–2017.
- Álvarez-Lao, D. J., Rivals, F., Sánchez-Hernández, C., Blasco, R. & Rosell, J. 2017: Ungulates from Teixoneres Cave (Moià, Barcelona, Spain): presence of cold-adapted elements in NE Iberia during the MIS3. *Palaeogeography, Palaeoclimatology, Palaeoecology* 466, 287–302.
- Antoine, P.-O. 2002: Phylogénie et évolution des Elasmotheriina (Mammalia, Rhinocerotidae). *Memoire du Muséum National d'Histoire Naturelle* 188, 1–359.
- Blumenbach, J. F. 1799: *Handbuch der Naturgeschichte*. 708 pp. Dieterich, Göttingen.
- Borsuk-Bialyncka, M. 1973: Studies on the Pleistocene rhinoceros *Coelodonta antiquitatis* (Blumenbach). *Paleontologia Polonica* 29, 1–148.
- Bronk Ramsey, C. 2009: Bayesian analysis of radiocarbon dates. *Radiocarbon* 51, 337–360.
- Bronn, H. G. 1837: *Lethaea geognostica, oder Abbildungen und Beschreibungen der für die Gebirgs Formationen bezeichnendsten Versteinerungen*. 1346 pp. E. Schweizerbart, Stuttgart.
- Chen, S., Deng, T., Hou, S., Shi, Q. & Pang, L. 2010: Sexual dimorphism in perissodactyl rhinocerotid *Chilotherium wimani* from the Late Miocene of the Linxia Basin (Gansu, China). *Acta Palaeontologica Polonica* 55, 587–597.
- Diedrich, C. G. 2008: A skeleton of an injured *Coelodonta antiquitatis* from the Late Pleistocene of north-western Germany. *Cranium* 25, 1–16.
- Dong, W., Hou, Y.-M., Yang, Z.-M., Zhang, L.-M. & Zhang, S.-Q. 2014: Late Pleistocene mammalian fauna from Wulanmulan Paleolithic Site, Nei Mongol, China. *Quaternary International* 347, 139–147.
- Fortelius, M., Mazza, P. & Sala, B. 1993: *Stephanorhinus* (Mammalia: Rhinocerotidae) of the western European Pleistocene, with a revision of *S. etruscus* (Falconer, 1868). *Palaeontographica Italica* 80, 63–155.
- Golubtsov, V. A. 2020: Stable carbon isotopic composition of organic matter of the Late Pleistocene and Holocene soils of the Baikal region. *Eurasian Soil Science* 53, 724–738.
- Gray, J. E. 1821: On the natural arrangement of vertebrate animals. *London Medical Repository* 15, 296–310.
- Groves, C. P. 1982: The skulls of Asian rhinoceroses: wild and captive. *Zoo Biology* 1, 251–261.
- Guérin, C. 1973: Les trois espèces de rhinoceros (Mammalia, Perissodactyla) du gisement Pléistocène Moyen des Abimes de la La Fage à Noailles (Corrèze). *Nouvelles Archives du Muséum d'Histoire Naturelle de Lyon* 11, 55–84.
- Guérin, C. 1980: Les rhinocéros (Mammalia, Perissodactyla) du Miocène terminal au Pléistocène supérieur en Europe occidentale: comparaison avec les espèces actuelles. *Documents des Laboratoires de Géologie de Lyon* 79, 1–1185.
- Guérin, C. 2010: *Coelodonta antiquitatis praecursor* (Rhinocerotidae) du Pléistocène moyen final de l'aven de Romain-la-Roche (Doubs, France). *Revue de Paléobiologie, Genève* (Décembre 2010) 29, 697–746.
- Handa, N., Izuho, M., Takahashi, K., Iizuka, F., Tsogetbaatar, B., Gunchinsuren, B., Odsuren, D. & Ishitseren, L. 2017: Discovery of a Late Pleistocene rhinocerotid from Ondorkhaan, eastern Mongolia. *The Journal of Geological Society of Japan* 123, V–VI (in Japanese).
- Hemming, S. 2003: Heinrich events: massive late Pleistocene detritus layers of the North Atlantic and their global climate imprint. *Reviews of Geophysics* 42, 1–43.
- Kahlke, H. D. 1977: Die Rhinocerotidenreste aus den Travertinen von Taubach. *Quartärpaläontologie* 2, 305–359.
- Kahlke, R. D. 2014: The origin of Eurasian Mammoth Faunas (*Mammuthus-Coelodonta* Faunal Complex). *Quaternary Science Reviews* 96, 32–49.
- Kahlke, R. D. & Lacombat, F. 2008: The earliest immigration of woolly rhinoceros (*Coelodonta tologojensis*, Rhinocerotidae, Mammalia) into Europe and its adaptive evolution in Palaearctic cold stage mammal faunas. *Quaternary Science Reviews* 27, 1951–1961.
- Kirillova, I. V., Olga, F., van der Made, C. J., Kukarckih, V. V., Shapiro, B., van der Plich, J., Shidlovskiy, F. K., Heintzman, P. D., van Kolfschoten, T. & Zanin, O. G. 2017: Discovery of the skull of *Stephanorhinus kirchbergensis* (Jäger, 1839) above the Arctic Circle. *Quaternary Research* 88, 1–14.
- Kosintsev, P., Mitchell, K. J., Devière, T., van der Plicht, J., Kuitens, M., Petrova, E., Tikhonov, A., Higham, T., Comeskey, D., Turney, C., Cooper, A., van Kolfschoten, T., Stuart, A. J. & Lister, A. M. 2019: Evolution and extinction of the giant rhinoceros *Elasmotherium sibiricum* sheds light on late Quaternary megafaunal extinctions. *Nature Ecology & Evolution* 3, 31–38.
- Lobachev, Y. V., Shpansky, A. V., Bondarev, A. A., Lobachev, A. Y., Vasiliev, S. K., Klementev, A. M., Grebnev, I. E. & Silaev, V. I. 2021: New findings of *Stephanorhinus kirchbergensis* in Siberia. *Palaeontologia Electronica* 24, a14, <https://doi.org/10.26879/734>.

- Loose, H. 1975: Pleistocene Rhinocerotidae of W. Europe with reference to the recent two-horned species of Africa and S.E. Asia. *Scripta Geologica* 33, 1–59.
- Lu, X., Deng, T., Zheng, X. & Li, F. 2020: Sexual dimorphism and body reconstruction of a hornless rhinocerotid, *Plesiaceratherium gracile*, from the early Miocene of the Shanwang Basin, Shandong, China. *Frontiers in Ecology and Evolution* 8, 544076, <https://doi.org/10.3389/fevo.2020.544076>.
- Mallet, C., Cornette, R., Billet, G. & Houssaye, A. 2019: Interspecific variation in the limb long bones among modern rhinoceroses—extent and drivers. *PeerJ* 7, e7647, <https://doi.org/10.7717/peerj.7647>.
- Markova, A. K. & Puzachenko, A. Y. 2007: Late Pleistocene mammals of Northern Asia and Eastern Europe. In Elias, S. A. (ed.): *Vertebrate Records. Encyclopedia of Quaternary Science* 4, 3158–3174. Elsevier, Amsterdam.
- Markova, A. K., Yu, A. & van Kolfschoten, T. 2010: The North Eurasian mammal assemblages during the end of MIS 3 (Brianskian–Late Karginian–Denekamp Interstadial). *Quaternary International* 212, 149–158.
- Mead, A. J. 2000: Sexual dimorphism and paleoecology in *Teleoceras*, a north American Miocene rhinoceros. *Paleobiology* 26, 689–706.
- Mihlbachler, M. C. 2007: Sexual dimorphism and mortality bias in a small Miocene North American rhino, *Menoceras arikarensis*: insights into the coevolution of sexual dimorphism and sociality in rhinos. *Journal of Mammal Evolution* 14, 217–238.
- Owen, R. 1848: *The Archetype and Homologies of the Vertebrate Skeleton*. 203 pp. John van Voorst, London.
- Pandolfi, L. 2018: Evolutionary history of Rhinocerotina (Mammalia, Perissodactyla). *Fossilias* 2018, 26–32.
- Pandolfi, L. & Petronio, C. 2011: The small-sized rhinoceroses from the Late Pleistocene of Apulia (southern Italy). *Rivista Italiana di Paleontologia e Stratigrafia* 117, 509–520.
- Pandolfi, L. & Tagliacozzo, A. 2015: *Stephanorhinus hemitoechus* (Mammalia, Rhinocerotidae) from the Late Pleistocene of Valle Radice (Sora, Central Italy) and re-evaluation of the morphometric variability of the species in Europe. *Geobios* 48, 169–191.
- Pandolfi, L., Bartolini-Lucenti, S., Cirilli, O., Bukhsianidze, M., Lordkipanidze, D. & Rook, L. 2021: Paleocology, biochronology, and paleobiogeography of Eurasian Rhinocerotidae during the Early Pleistocene: the contribution of the fossil material from Dmanisi (Georgia, Southern Caucasus). *Journal of Human Evolution* 156, 103013, <https://doi.org/10.1016/j.jhevol.2021.103013>.
- Qiu, Z.-X., Deng, T. & Wang, B.-Y. 2004: Early Pleistocene mammalian fauna from Longdan, Dongxiang, Gansu, China. *Palaeontologia Sinica New Series* C 27, 1–198.
- Reimer, P. & 41 others. 2020: The IntCal20 Northern Hemisphere radiocarbon age calibration curve (0–55 cal kBP). *Radiocarbon* 62, 725–757.
- Rey-Iglesia, A., Lister, A. M., Stuart, A. J., Bocherens, H., Szipak, P., Willerslev, E. & Lorenzen, E. D. 2021: Late Pleistocene paleoecology and phylogeography of woolly rhinoceroses. *Quaternary Science Reviews* 263, 106993, <https://doi.org/10.1016/j.quascirev.2021.106993>.
- Schvyreva, A. K. 2016: *The Elasmotherii of Pleistocene Eurasia*. 218 pp. Pechatniy Dvor Publishers, Stavropol (in Russian).
- Schwartz-Narbonne, R., Longstaffe, F. J., Kardynal, K. J., Druckenmiller, P., Hobson, K. A., Jass, C. N., Metcalfe, J. Z. & Zazula, G. 2019: Reframing the mammoth steppe: insights from analysis of isotopic niches. *Quaternary Science Reviews* 215, 1–21.
- Shpansky, A. V. & Billia, E. M. E. 2012: Records of *Stephanorhinus kirchbergensis* (Jäger, 1839) (Mammalia, Rhinocerotidae) from the Ob' River at Kransy Yar (Tomsk region, southeast of Western Siberia). *Russian Journal of Theriology* 11, 47–55.
- Shuang, X.-Y., Yuan, J.-X., Hou, X.-D., Sheng, G. L., Yin, J. & Lai, X.-L. 2012: Ancient DNA analysis of woolly rhinoceros in Xiaogu Mountain, Haicheng City, Liaoning Province. *Geological Science and Technology Information* 31, 40–44.
- Stuart, A. J. & Lister, A. M. 2012: Extinction chronology of the woolly rhinoceros *Coelodonta antiquitatis* in the context of late Quaternary megafaunal extinctions in northern Eurasia. *Quaternary Science Reviews* 51, 1–17.
- Takahashi, K., Wei, G., Uno, H., Yoneda, M., Jin, C., Sun, C., Zhang, S. & Zhong, B. 2007: AMS <sup>14</sup>C chronology of the world's southernmost woolly mammoth (*Mammuthus primigenius* Blum.). *Quaternary Science Reviews* 26, 954–957.
- Tong, H.-W. 2012: Evolution of the non-*Coelodonta dicerorhine* lineage in China. *Comptes Rendus Palevol* 11, 555–562.
- Tong, H.-W. & Moigne, A.-M. 2000: Quaternary rhinoceros of China. *Acta Anthropologica Sinica* 19, 257–263.
- Tong, H.-W., Chen, X. & Zhang, B. 2018: New postcranial bones of *Elasmotherium peii* from shanshenmiaozui in Nihewan Basin, Northern China. *Quaternaire* 29, 195–204.
- Tong, H.-W., Wang, F., Zheng, M. & Chen, X. 2014: New fossils of *Stephanorhinus kirchbergensis* and *Elasmotherium peii* from the Nihewan Basin. *Acta Anthropologica Sinica* 33, 369–388.
- Tseveendorj, D., Batbold, N. & Amgalantugs, T. 2006: *Mongolanthropus* was discovered in Mongolia. *Studia Archeologica. Institutii Archaeologici Academiae Scientiarum Mongoloeae (III)* 23, 5–10 (in Mongolian).
- van der Made, J. 2010: The rhinos from the Middle Pleistocene of Neumark Nord (Saxony-Anhalt). *Veröffentlichungen des Landesamtes für Archäologie* 62, 432–527.
- Vercoutère, C., Guérin, C., Crépin, L., Richarin, P., Gandolfo, N., Vincent, J., Marsac, J., Cersoy, S., Rousselière, H., Walter, P., Brunelle, A., Nowik, W., Brissaud, D., Drucker, D. G., van der Plicht, J., Patou-Mathis, M. & Vialet, A. 2013: Étude pluridisciplinaire du squelette de rhinocéros laineux, *Coelodonta antiquitatis* (Blumenbach, 1799), de l'Institut de paléontologie humaine (Paris, France). *L'Anthropologie* 117, 1–47.
- Waters, M. R. & Stafford Jr, T. W. 2007: Redefining the age of Clovis: implications for the peopling of the America. *Science* 315, 1122–1126.

## Supporting Information

Additional Supporting Information may be found in the online version of this article at <http://www.boreas.dk>.

*Fig. S1.* Skeletal reconstruction of the rhinocerotid from Ondorkhaan, Mongolia (modified from Vercoutère *et al.* 2013). Grey colour indicates preserved parts.

*Fig. S2.* Ribs. A. Right side ribs. B. Left side ribs. C. Possible healed bone fracture. Scale bar represents 10 cm.

*Fig. S3.* Metrical comparison between selected postcrania of H.E.M 2012.24.1 and four Late Pleistocene northern Eurasian rhinocerotid species. Data sources: for *Coelodonta antiquitatis* (Borsuk-Bialyncka 1973; Guérin 1980; present study); *Elasmotherium sibiricum* (Schvyreva 2016); *Stephanorhinus kirchbergensis* (Kahlke 1977; Guérin 1980; Fortelius *et al.* 1993); and for *Stephanorhinus hemitoechus* (Guérin 1980; Fortelius *et al.* 1993).

*Fig. S4.* A–E. Morphological comparison of distal part of the radius between H.E.M 2012.24.1 and late Pleistocene rhinocerotids from northern Eurasia. F–J. Morphological comparison of cranial side of the lunate between H.E.M 2012.24.1 and late Pleistocene rhinocerotids from northern Eurasia. A. H.E.M 2012.24.1. B. *Coelodonta antiquitatis* (modified after Diedrich 2008). C. *Elasmotherium sibiricum* (modified

after Schvyreva 2016). D. *Stephanorhinus kirchbergensis* (modified after Fortelius *et al.* 1993). E. *Stephanorhinus hemitoechus* (modified after van der Made 2010). F. H.E.M 2012.24.1. G. *Coelodonta antiquitatis* (modified after Guérin 1980). H. *Elastotherium sibiricum* (modified after Schvyreva 2016). I. *Stephanorhinus kirchbergensis* (modified after

Guérin 1980). J. *Stephanorhinus hemitoechus* (modified after Guérin 1980). Abbreviation: Rsp = radial styloid process.

*Table S1.* Metrical comparison between postcrania of H.E.M 2012.24.1 and adequately described specimens of *Coelodonta antiquitatis* (in mm).